# Rifting Processes at a Continent-Ocean Transition Rift Revealed by Fault Analysis: Example of Dabbahu-Manda-Hararo Rift (Ethiopia)

Stephanie Dumont, Yann Klinger, Anne Socquet, Javier Escartin, R. Grandin, E. Jacques, S. Medynski, C Doubre

Tectonics

RESEARCH ARTICLE
10.1029/2018TC005141

**Key Points:**
- Fault analysis, density map, and strain analysis are performed for 668 normal faults
- Magmato-tectonic evolution of the rift is proposed for the last 100 kyr
- Rift-ocean ridges are compared to unravel the behavior of a continent-ocean transition rift

**Supporting Information:**
- Supporting Information S1

**Correspondence to:**
S. Dumont,
sdumont@segal.ubi.pt

**Citation:**
Dumont, S., Klinger, Y., Socquet, A., Escartín, J., Grandin, R., Jacques, E., et al. (2019). Rifting processes at a continent-ocean transition rift revealed by fault analysis: Example of Dabbahu-Manda-Hararo rift (Ethiopia). *Tectonics*, *38*. https://doi.org/10.1029/2018TC005141

Received 10 MAY 2018
Accepted 30 NOV 2018
Accepted article online 6 DEC 2018



# Rifting Processes at a Continent-Ocean Transition Rift Revealed by Fault Analysis: Example of Dabbahu-Manda-Hararo Rift (Ethiopia)

**S. Dumont[1,2], Y. Klinger[1], A. Socquet[3], J. Escartín[1], R. Grandin[1], E. Jacques[1], S. Medynski[4,5], and C. Doubre[6]**

[1]Institut de Physique du Globe de Paris, Sorbonne Paris Cité, CNRS, Paris, France, [2]Instituto Dom Luiz, Universidade da Beira Interior, Covilhã, Portugal, [3]University Grenoble Alpes, University Savoie Mont Blanc, CNRS, IRD, IFSTTAR, Grenoble, France, [4]CRPG UMR 7358 CNRS, Université de Lorraine, Vandoeuvre-lès-Nancy, France, [5]Cerema, Direction Technique Infrastructures de Transport et Matériaux, Provins, France, [6]Université de Strasbourg, IPGS, Strasbourg, France

**Abstract** Analyses of fault attributes have contributed to unraveling fault growth processes in diverse tectonic settings. By integrating such analysis at the scale of a fault population, we propose to investigate the characteristics of a rift that has evolved up to a stage typical of a continent-ocean transition. We address this problem by considering Dabbahu-Manda-Hararo (DMH) rift segment (Central Afar, Ethiopia), recognized for being in a late rifting stage. We quantify fault azimuth, length, and throw attributes for 668 normal faults. Along DMH rift, the mean fault density is 0.87 ± 0.7 km/km$^2$ and the median tectonic strain ranges from 1.8% to 3.1% assuming a fault dip of 60° and 45°, respectively. Maximum tectonic strain (>10%) is found where the rift azimuth changes. Along-rift variations in fault azimuth, length, and scaling relationships suggest a different stage of rifting in the northern part of the rift. We show that this difference can be attributed to the influence of the Dabbahu volcano located at the northern tip of the rift, which captured the propagating Manda-Hararo rift in the last ~100 kyr. The morpho-tectonic analysis reveals numerous common features with slow-spreading ridge segments, such as the Lucky Strike segment located along the Mid-Atlantic ridge (segment length, spreading rate, associated magmatic system) but also with intermediate and fast ones (axial valley, fault throws, and diking). This study reveals that a rift at the continent-ocean transition may be characterized by a transient and evolutionary behavior that shares features with oceanic ridges from slow- to fast-spreading rates.

**Plain Language Summary** East Africa forms one of the best locations around the world for studying rifting processes. In the Afar depression, three limits of tectonic plates meet to break up the African continent. Faults and volcanism shape rift morphology, and they both participate in the continental breakup. We study 668 faults along the Dabbahu-Manda-Hararo rift that is close to give birth to an ocean. We focus on how faults develop by measuring their length, their height, orientation, and number in a given area. Our analysis shows that in the northern part of the rift, faults develop in a singular way, illustrated by their unusual great length at the rift axis. We gather evidences of the specificity of faults located in this area, and we link them to the presence of Dabbahu volcano that developed ~100 kyr ago in this area. We also compare our rift to a slow oceanic ridge located in Atlantic with which it shares numerous features (spreading rate, morphology, and magmatic system). This comparison leads us to discuss how different these extensional systems are and to better understand the transition between a continent and an ocean.

## 1. Introduction

The formation and development of fractures and faults under tectonic forces accommodate strain within the brittle crust at scales ranging from millimeters to kilometers. In extensional environments, fault analyses over a wide range of spatial and temporal scales provide insights into the physical mechanisms and conditions of fault growth as well as fault evolution (Cartwright et al., 1995; Cowie & Scholz, 1992a; Dauteuil et al., 2001; Manighetti, King, et al., 2001; Perrin et al., 2016). Among the various approaches addressing these processes, studies have evaluated fault attributes such as fault azimuth, length, cumulative displacement, spacing, or damage zone width, to characterize a fault population using a collection of individual fault

segments (Kolyukhin & Torabi, 2012; Soliva & Schultz, 2008; Torabi & Berg, 2011). Besides testing models of fault growth, these quantitative parameters and their variations are also useful to estimate tectonic strain and to decipher the role of faulting in shaping the topography (e.g., Cowie et al., 1993; De Chabalier & Avouac, 1994; Deschamps et al., 2005, 2007). This approach has been widely used to investigate the growth of fault populations as a result of rifting or oceanic spreading processes (e.g., Bohnenstiehl & Carbotte, 2001; Deschamps et al., 2005, 2007).

Studies of continental rifts, volcanic and non-volcanic passive margins using a wide range of techniques from observations to numerical modeling have greatly improved our understanding of the different stages of continental rifting leading to continental breakup. In magmatic context, the respective role of tectonics and magmatism and their interactions is more complex to evaluate (Acocella, 2014; Bastow & Keir, 2011; Behn et al., 2002; Buck, 2004; Corti, 2012; Courtillot, 1982; Didana et al., 2014; Ebinger & Casey, 2001; Geoffroy, 2005; Hayward & Ebinger, 1996; Kusznir & Karner, 2007; Liao & Gerya, 2015; Rooney et al., 2014; Stab et al., 2016). Buck (2004) showed that with magmatism the tectonic forces required to separate two plates are about one tenth compared to amagmatic rifting. In addition to facilitating plate separation, dike intrusions progressively modify the thermal and compositional structure of the continental lithosphere, which is thinned during the continent-ocean transition.

The transition from continental rifting to oceanic spreading is accompanied by an increase in magmatism at the expense of faulting (Hayward & Ebinger, 1996), making magmatism the main process accommodating the extension between tectonic plates (Ebinger & Casey, 2001). The role of faulting and its interaction and partitioning with magmatism during continental breakup have been addressed through multiple studies (Acocella, 2014; Behn et al., 2002; Belachew et al., 2013; Casey et al., 2006; Corti et al., 2003; Ebinger & Casey, 2001; Ebinger et al., 2017; Hayward & Ebinger, 1996). In particular, many studies have focused on the faults of the East African Rift System (EARS) and the Afar depression to quantify the amount of tectonic strain (i.e., stretching and thinning) with respect to magma intrusion (Acocella et al., 2008; Agostini et al., 2011; Corti, 2012; Gupta & Scholz, 2000; Keir et al., 2006, 2009; Manighetti, King, et al., 2001) in the overall process of continental breakup. For continental magmatic rifts, the few estimates of the tectonic strain accommodated by faults show a relatively wide range of values, between a few percent and 15% (De Chabalier & Avouac, 1994; Gupta & Scholz, 2000). Beyond the techniques used, such variations provide insights about the different stages of rifting, as well as the variations in faulting along the rift axis. Is the strain released in a similar way at the magmatic center and rift tips? How similar a fault population of a continent-ocean transition rift is to those of oceanic ridges? What does this similarity imply for the continental breakup? To address these questions, the continental rift of Dabbahu-Manda-Hararo (DMH) located in Ethiopian Afar is among the best candidates to properly characterize the nature of faulting during the continent-ocean transition and onset of seafloor spreading. In a late stage of rifting, the DMH rift has hosted an intrusive sequence of 14 dikes between 2005 and 2010 (Wright et al., 2012) that have reshaped the rift topography by both fault activation and effusive volcanism (Barnie et al., 2016; Dumont et al., 2016; Ferguson et al., 2010; Grandin et al., 2009; Hamling et al., 2009; Rowland et al., 2007). Situated in an arid region, fault scarps along the DMH rift are well protected from erosion (Stein et al., 1991), thus allowing detailed analysis of displacement-length (D-L) profiles (Dumont et al., 2017). Although Dumont et al. (2017) considered 357 normal faults along the DMH rift, they restricted the study to the shapes of D-L profiles, thus providing only insights on long-term lateral fault propagation in a magma-rich rift.

Here we characterize 668 individual fault segments using several fault attributes including geometry, fault trace, and vertical throws, to shed lights on fault growth processes and strain distribution, as well as their variations along DMH rift. The DMH rift geometry and in particular the change of azimuth of the main axis and associated fault network, impact the process of fault growth and its evolution. Furthermore, recent studies have shown magmato-tectonic interactions at the northern rift tip involving the Dabbahu stratovolcano (Ayele et al., 2007; Dumont et al., 2016; Grandin et al., 2009; Medynski et al., 2013, 2016; Wright et al., 2006), leading us to consider the potential interplay between the fault population and the volcano on the process of fault growth and its evolution. Integrating the results of fault attribute analyses at the rift scale leads us to propose a conceptual model to describe the DMH rift evolution. To further explore the behavior of the ocean-continent transition rift, we compare our morpho-structural analyses and subsequent strain estimates to those for oceanic ridges. To this end, we consider Lucky Strike, a slow oceanic spreading center (North

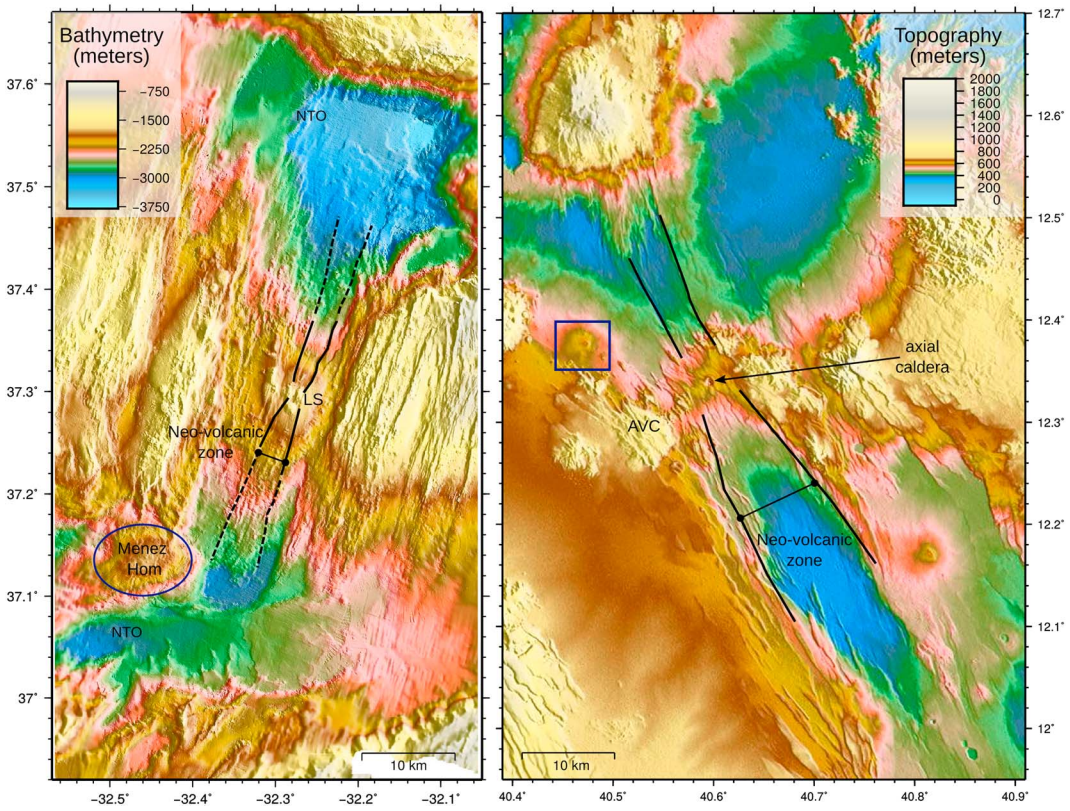


**Figure 1.** Morphological comparison between Lucky Strike oceanic spreading segment (left) and Dabbahu-Manda-Hararo rift (right). A similar color scale allows to emphasize similarities between the two systems such as the transversal volcanic constructs that are rifted by normal faults. The borders of the neovolcanic zones (rift valley) are delimited by black lines. At Dabbahu-Manda-Hararo rift, off-axis volcanism is shown using blue rectangle (Dessisa et al., 2013; Medynski et al., 2015). At Lucky Strike oceanic spreading segment, the Menez Hom relief is associated with ultramafic rocks and the nontransform offsets (NTO) are characterized by complex structures with faulting, tectonic rotation, and uplift (Escartín et al., 2014).

Atlantic) that shares features (spreading rate, morphology, and magma plumbing system) with DMH rift (Figure 1 and Table 2) and where magmato-tectonic processes have been well characterized (e.g., Cannat et al., 1999; Escartín et al., 2014). This detailed comparison offers an opportunity to better capture specificities of a late stage of continental breakup.

## 2. Tectonic Setting

The Afar Depression is a diffuse triple junction where the Gulf of Aden (GA) oceanic ridge and the Red Sea (RS) rift systems, overlap in Central Afar and meet the EARS (Figure 2a; Barberi & Varet, 1977; Ehrhardt & Hübscher, 2015; Manighetti, Tapponnier, et al., 2001). Along the three rift branches, extension and volcanism are concentrated along rift segments (Casey et al., 2006; Hayward & Ebinger, 1996). This triple junction formed after the flood basalt magmatism known as Ethiopian-Yemen traps, dated about 30 ± 1 Myr ago (Hofmann et al., 1997) and that led to rifting in the region (Courtillot et al., 1999; Ebinger et al., 2017). This continental breakup is characterized by a period of distributed stretching, ~29 to 26 Myr ago, followed by a period of thinning, from 23 Myr to ~7 Myr (Stab et al., 2016, and references therein). A late phase of flood basalt, known as the "Stratoid series," occurred from ~1 to ~4 Myr ago and covered about two thirds of the Afar depression (Lahitte et al., 2003, and references therein). At the top of the Stratoid series between ~1.1 and ~0.6 Myr, a new form of volcanism, known as the "Gulf Basalt" formation, developed. The Gulf Basalts are characterized by the localized emission of basaltic lava flows along large faults dissecting massive silicic centers (Kidane et al., 2003; Stab et al., 2016). This formation is recognized as part of a regional localizing phase (Stab et al., 2016). The mantle seismic velocity structure underlying the Afar depression reveals narrow low-velocity zones below the rift segments, interpreted as segmented mantle upwelling beneath Afar

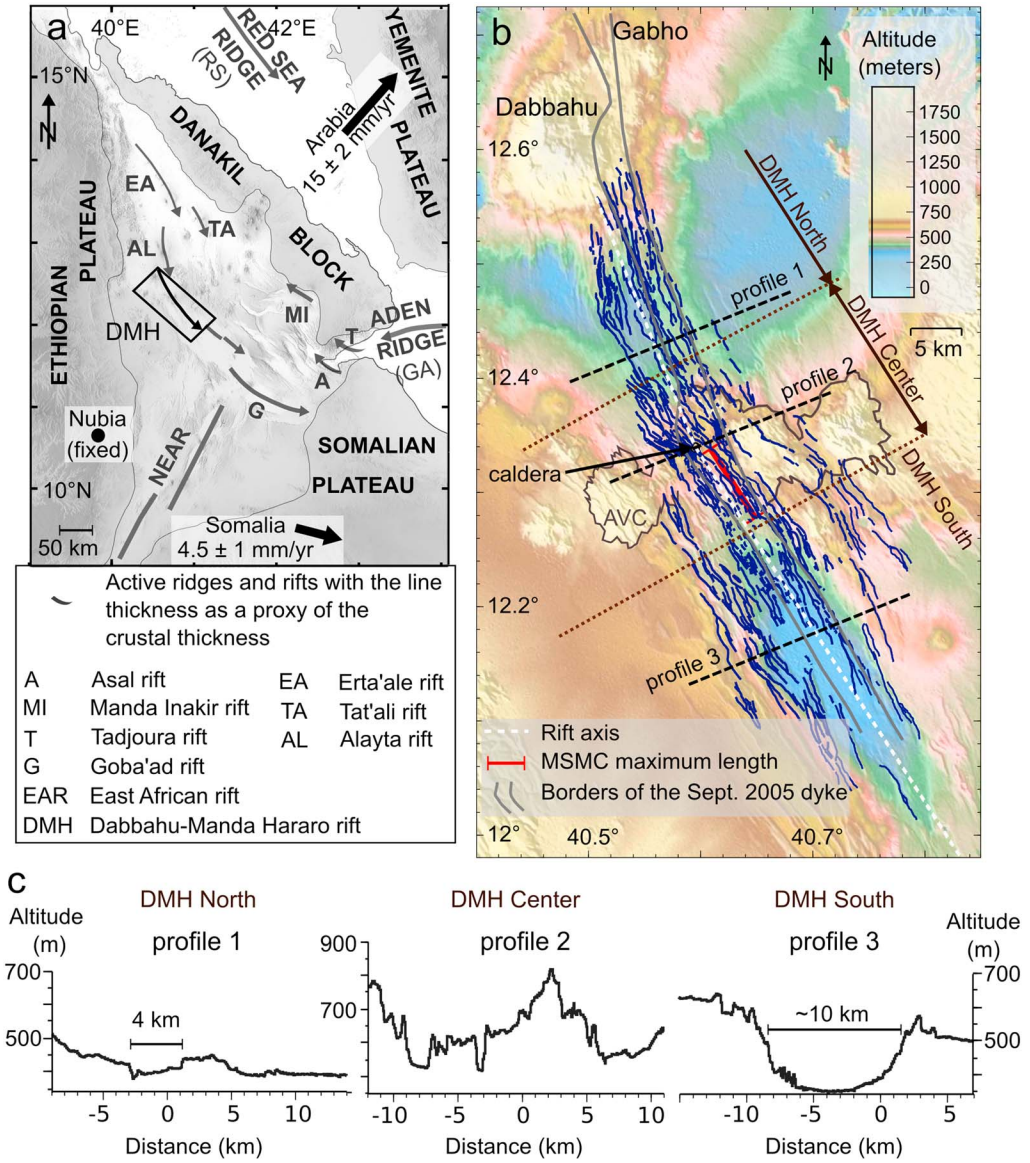


**Figure 2.** magmato-tectonic setting of Dabbahu-Manda-Hararo (DMH) rift. (a) magmato-tectonic rifts composing the three branches of the Afar triple junction, the Red Sea and Aden ridges as well as the system of the east African rifts. The arrows associated to rift segments represent the direction of rift propagation. After Figure 26 from Manighetti, Tapponnier, et al. (2001). (b) Topographic map of DMH rift including the mapping of the 668 faults considered in this study (blue lines). In addition to the mid-segment magma chamber, other magma sources are also indicated: Ado'Ale volcanic complex, Dabbahu and Gabho volcanoes. Along the rift axis, three rift segments are defined (north, center, and south, dark brown dotted lines) based on morphological and structural observations (see text for more details). Topographic profiles (black dashed lines) across these three segments are shown in (c).

(Gallacher et al., 2016; Hammond et al., 2013). The narrowing and localization of deformation are attributed to variations in magma supply and volatiles that directly impact the lithosphere rheology (Ebinger et al., 2017; Stab et al., 2016). Using tectonic observations and geochronological measurements along the Asal-Ghoubbet and Manda Inakir rifts, Manighetti et al. (1998) proposed that the GA ridge is propagating northwestward on land, following the western boundary of the continental Danakil block (Figure 2a). Combining multi-scale observations and geometrical and mechanical arguments, they also suggested a southeastward propagation of the RS rift segments, primarily controlled by the minimum horizontal principal stress. Moreover, an analysis of along-axis segmentation revealed an evolutionary sequence from early continental rifting to incipient seafloor spreading (Chorowicz, 2005; Hayward & Ebinger, 1996). From EARS to Afar, there is an increase in extension and magmatism that is linked to a decrease in the

segment length, fault dimension, elastic and lithospheric thicknesses (supporting information Table S1; Casey et al., 2006; Ebinger et al., 2017; Hammond et al., 2011; Hayward & Ebinger, 1996; Kogan et al., 2012). Similarly, crustal anisotropy increases from EARS to Afar. The magnitude of anisotropy is higher along Quaternary-Recent rift segments where strain is accommodated by magmato-tectonic processes (Keir et al., 2011). Finally, the margin subsidence associated with a voluminous emission of basalts in a heavily intruded and weakened plate characterizes the ultimate stage of thinning (Bastow & Keir, 2011). This latest stage, which precedes the onset of seafloor spreading, was only evidenced in the northernmost part of Afar.

Located along the RS ridge, the DMH rift consists of a ~60-km-long and ~20-km-wide volcano-tectonic segment where faulting and volcanism have been localized since ~1.0–1.5 Myr (Audin et al., 2004). Following the emplacement of the Gulf Basalt formation, the magmato-tectonic activity decreased significantly in relation to the northward inland Aden-Ghoubbet rift propagation (Acocella et al., 2008; Audin et al., 2004). After 0.2 Myr, the accumulated strain turned to be released through short but intense and localized phases of magmatism, as illustrated by the last 2005–2010 rifting episode (Stab et al., 2016; Wright et al., 2012). The DMH rift accommodates most of the 15 mm/year divergence between Nubia and Arabia plates (Figure 2a; e.g., Vigny et al., 2006). Similar to other rift segments in Afar, the DMH rift hosts at its center a silicic volcanic complex, the Ado'Ale Volcanic Complex (AVC), which has been intensely dismantled by large normal faults (Figures 1, 2b, and 2c; Lahitte, Gillot, & Courtillot, 2003; Lahitte, Gillot, Kidane, et al., 2003). Widespread deformation and high density of short faults in this area characterize long-term magmato-tectonic interactions (Dumont et al., 2017). The location of the AVC also coincides with a change in rift azimuth. South of AVC, the main graben and normal faults are oriented ~N150°, and therefore orthogonal to the N055° extension direction of the Arabia/Nubia divergence, while North of AVC the tectonic structures are oriented N165° (Figure 2b; Rowland et al., 2007).

At its northern tip, the DMH rift hosts the ~10 km in diameter Dabbahu stratovolcano (Figure 2b). The effusive activity of this volcano was particularly intense 72–58 kyr ago, when it resurfaced the topography north of AVC (Medynski et al., 2013). Its plumbing system may include a series of stacked sills at depths ranging from 1 to 5 km, based on petrogeochemical and geophysical analyses and point toward the existence of a long-lived underlying magma storage (Field et al., 2012). Moreover, geodetic and seismic data have shown that both the Dabbahu and the nearby Gabho volcano (Figure 2b) were involved in the first and longest dike intrusion (~60-km long) of the 2005–2010 rifting episode, explaining why the first and largest dike intruded the eastern rift shoulder north of AVC (Grandin et al., 2009).

At the rift center, a magmatic system, later named "mid-segment magma chamber" or MSMC (Figure 2b), was identified during the last rifting episode as the main feeder of the dikes injected between June 2006 and May 2010 (Belachew et al., 2011; Grandin et al., 2010; Hamling et al., 2009; Wright et al., 2012). Although shifted ~5 km southward with respect to the axial position of AVC (Figure 2), MSMC belongs to AVC's magma plumbing system located at the rift center (Dumont et al., 2017). In the following sections, we will not discriminate MSMC from AVC when dealing with the long-term magmatic plumbing system at the rift center. In that case, we will use the name AVC. Magmato-tectonic interactions have also been observed around MSMC over months following dike intrusions in connection with transient surface deformation caused by refilling processes in the shallow magma chamber (Dumont et al., 2016; Grandin et al., 2010). In addition, recent geodetic studies have shown that viscoelastic relaxation could not explain alone the high-rate displacements measured in the years following the rifting episode suggesting that magma kept playing a key role in the surface deformation (Hamling et al., 2014; Pagli et al., 2014).

## 3. Material and Methods

To characterize fault growth processes both at the fault and rift scales, we quantify fault attributes through detailed fault mapping. Mapping was performed using various data sets (see supporting information, Figure S1), including panchromatic Quickbird images (with a 60-cm ground resolution), SPOT-5 images (2.5-m resolution), and a 10-m-accuracy DEM generated from SPOT-5 stereo images (20-m resolution). These data sets were complemented by Interferometric Synthetic Aperture Radar (InSAR) images spanning the post-September 2005 period (20-m resolution). Eventually, a total of 668 faults were mapped along DMH rift (Figure 2b; Dumont et al., 2016). This structural map extends primarily over the neovolcanic zone (<0.6

Myr) and also over the Gulf Basalt series (1.1–0.6 Myr) composing the rift flanks including the AVC (Kidane et al., 2003; Stab et al., 2016). The oldest dating of fault scarp available on the rift eastern flank goes back to ~200 kyr (Ferguson et al., 2013), a time interval we tackle with this study. Our fault mapping includes the most recent magmato-tectonic events up to May 2007, the date of the latest optical images used for this map (Figure 2b; Dumont et al., 2016). Recent volcanism (<2 kyr) in the rift center prevented us from identifying numerous of the most recent tectonic structures there (Ferguson et al., 2010). The two eruptions of August 2007 and June 2009 covered areas of 2.2 and 4.5 $km^2$ respectively, south of the center of MSMC (~12.25°N, 40.67°E), likely covering faults (Ferguson et al., 2010). In May 2010, the smaller and latest lava field of the 2005–2010 rifting episode ($0.23 \times 10^6$ $m^3$) formed, ~10 km north of these two eruptions (~12.33°N, 40.62°E, Barnie et al., 2016), covering a part of a >11-m-high fault we mapped.

We measured the following fault parameters: along-strike vertical throws, length, and azimuth. Fault strike is defined from the end points of each individual fault, since most faults are overall linear. Scarp heights were measured through a series of short profiles perpendicular to local fault strike, spaced laterally by ~15 m along the fault length. For each profile, the scarp height was quantified by subtracting the elevation of the bottom from the elevation of the top of the fault scarp, which were estimated by fitting linear regressions of the topographic slopes on each side of the fault (Dumont et al., 2016). Fault map was also used to compute the fault density along DMH rift. Fault density was measured as the cumulative fault length per area, using a $1 \times 1$ $km^2$ sliding window with a 500-m overlap, a method that was also used along the slow-spreading Lucky Strike ridge segment (Escartín et al., 2014).

Following Bohnenstiehl and Carbotte (2001), we have estimated the strain accommodated by normal faults across the rift to evaluate the role of faulting in rifting processes. We calculate the cumulative sum of all vertical scarp heights along profiles normal to the rift starting from the morphological rift axis (white dotted line, Figures 2b and 5a). Horizontal extension can be calculated assuming a fault dip. The calculated strain (horizontal strain divided by profile length) is thus influenced by fault angle (see supporting information, Figure S2). At the DMH rift segment, analysis of focal mechanisms for $Mw > 3.5$ earthquakes during the propagation of the November 2007 and October 2008 dikes suggests mean fault dips of 62.2° ± 9.7° (Belachew et al., 2013). We therefore reduced the range of fault dips to two end-member dips, 45° and 60° to calculate strain along profiles. These fault dips are actually also used in other similar studies (e.g., Bohnenstiehl & Carbotte, 2001; Combier et al., 2015), thus facilitating comparison of results from different areas.

## 4. General Morphostructural Analysis of DMH Rift

We used along-axis morpho-tectonic changes to subdivide DMH rift into the north, center and south segments (Figure 2b). The geomorphology of the north segment is characterized by a change in the rift azimuth (N165° instead of N150°) that takes place between N12.35° and N12.45°, north of AVC (Figure 2b; Dumont, 2013). There, the rift axis is much less prominent than elsewhere along the rift (Figures 2b and 2c). The rift valley is mostly asymmetrical (west dipping faults) and narrow (maximum width ~4 km and depth ~50 m). The north segment is considered as a representative of the interaction between Manda-Hararo (MH) rift and Dabbahu volcano (Figure 2c; Medynski et al., 2013, 2016). At the rift center, the prominent relief of AVC is intensely faulted, showing a transition zone between the northern and southern axial valley morphologies. Thus, the center segment is defined by a prominent topography (100–150 m) and a rift axis that is not so well-defined evidencing the interaction between the rift axis and the AVC (Figures 2b and 2c). The south segment of the rift corresponds to a well-defined and symmetrical rift axis (~10-km wide and ~100-m deep), in contrast with that of the north segment. In addition, normal fault scarps are subvertical all along the rift. Tilted blocks are absent along the rift margins, except very locally along the northeastern rift shoulder (north segment). Such absence of tilted block has been interpreted as the result of specific interactions between the local topography and dike intrusions at crustal depths (Dumont et al., 2016).

When comparing these morphological observations to the fault density map (Figure 3), two areas with relative high fault density appear: in the northern part of the north segment and at the rift center. In the north segment, the highest fault density exceeds 6 $km/km^2$ in the morphological axial depression. A high fault density, ~2–3 $km/km^2$, is also detected along the western flank of the graben formed in September 2005. These values reflect a dense population of long faults in this rift area, both along and off the rift axis (supporting information, Figure S3). At the rift center, the largest area with a high fault density, ~2–3 $km/km^2$, is

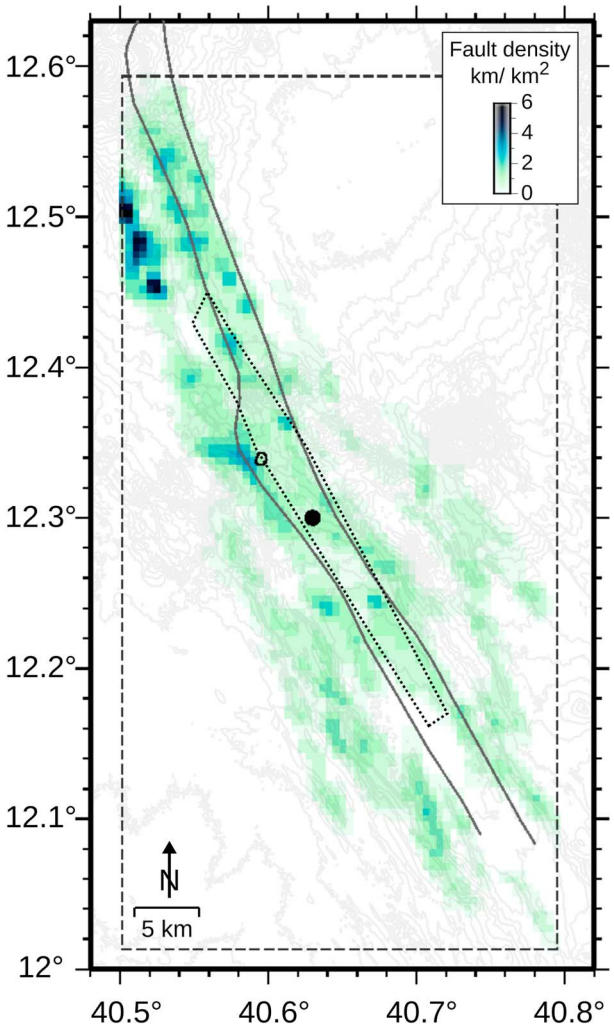


**Figure 3.** Fault density of the 668 faults mapped along the Dabbahu-Manda-Hararo rift. Fault density is measured as the cumulative fault length within 1 × 1 km boxes in the area defined by the dashed line. Dark gray lines represent the borders of the September 2005 dike-induced graben (after Grandin et al., 2009), the black filled circle indicates the mid-segment magma chamber center and the black oval the small caldera located at the rift axis. Dotted black line defines the area where the dikes from June 2006 to May 2010 emplaced. Light gray lines correspond to 10 m topographic contours.

observed on the northwestern side of the small caldera. In the center and south segments, fault densities with similar values are more scattered, but they tend to concentrate along the borders of the deforming area induced by the September 2005, and they may indicate areas where dikes intruded from AVC tend to be repeatedly emplaced. Further south, the fault density is lower, in particular, at the graben axis.

## 5. Fault Attribute Distribution and Scaling Laws

### 5.1. Fault Attributes

We consider here the distribution of fault azimuth and fault length along the rift. The rose diagram of fault orientation normalized by fault length (Figure 4a, left) reveals that the fault azimuth distribution shows along-rift axis variations. This is illustrated by the obliquity plot (azimuth deviation from the normal to the extension direction) for four groups of fault with different lengths (Figure 4a, right). The azimuth deviation is calculated with respect to the regional extension direction defined geodetically after Vigny et al. (2006). The highest obliquity values occur at rift tips, reaching 30–35° and 20–25° for the north and south rift segments, respectively. The smallest obliquity values are measured at the rift center in the narrow band, where magmatism has been localized for the last 20 kyr (Dumont et al., 2017), and also at the northernmost part of the rift (Figure 4a, right). The fault obliquity is thus increasing from the rift center toward both rift tips, although it is more pronounced northward (~21° per 0.1° of latitude) than southward (~21° per 0.1° of latitude). Faults with largest obliquity are located between the Dabbahu volcano and the AVC around ~12.5°N, where the rift shows also a change in azimuth. Fault azimuth appears to be subparallel to a line linking these two volcanic edifices (Figure 2b and supporting information, Figure S4). We also observe that faults with $L > 4$ km, which represent 10% of our fault population, are located both at the rift shoulders and at the rift axis in the north rift segment while they are most exclusively located at the rift shoulders elsewhere along the rift (supporting information, Figure S3).

### 5.2. Displacement-Length Relationship

The assumed relationship between the cumulative displacement ($D$) and fault length ($L$): $D = \gamma L^n$, includes $\gamma$, a parameter related to rock mechanical properties and $n$, the exponent reflecting the fault growth conditions ($1 \leq n \leq 2$; Scholz, 2002). This latter parameter means that mixing $D$-$L$ measurements from different fault systems might likely contribute to the scattering of $D$-$L$ relationship (Cowie & Scholz, 1992b; Kim & Sanderson, 2005; Torabi & Berg, 2011). Therefore, we chose to compare our measurements only with data from the Afar region (Figure 4b) because of the similarity of tectonic regimes and crustal materials (Ebinger & Hayward, 1996; Hammond et al., 2011, 2013; Manighetti et al., 1998; Manighetti, Tapponnier, et al., 2001; Redfield et al., 2003). Hence, we used data from Manighetti, King, et al. (2001) that includes faults from (1) Asal-Ghoubbet rift, with Asal representing the "inland" and Ghoubbet the "submarine" parts of the termination of the propagating Aden oceanic ridge, both being among the most recent and active rift segments of the Afar depression where magmatism and faulting accommodate most of the extension; (2) Central Afar of which 90% of the faults are from the center of the Afar depression and 10% of the faults are from the northern tip of EAR. These faults are associated with a more distributed deformation than that along rift segments and are not related to any kind of volcanism. These faults do not accommodate more than 15% of the total strain, although they include some of the larger, older (~2 Myr), and less active faults (≤1–2 mm/year) identified in the area. Figure 4b shows significant scattering in the data, which is common

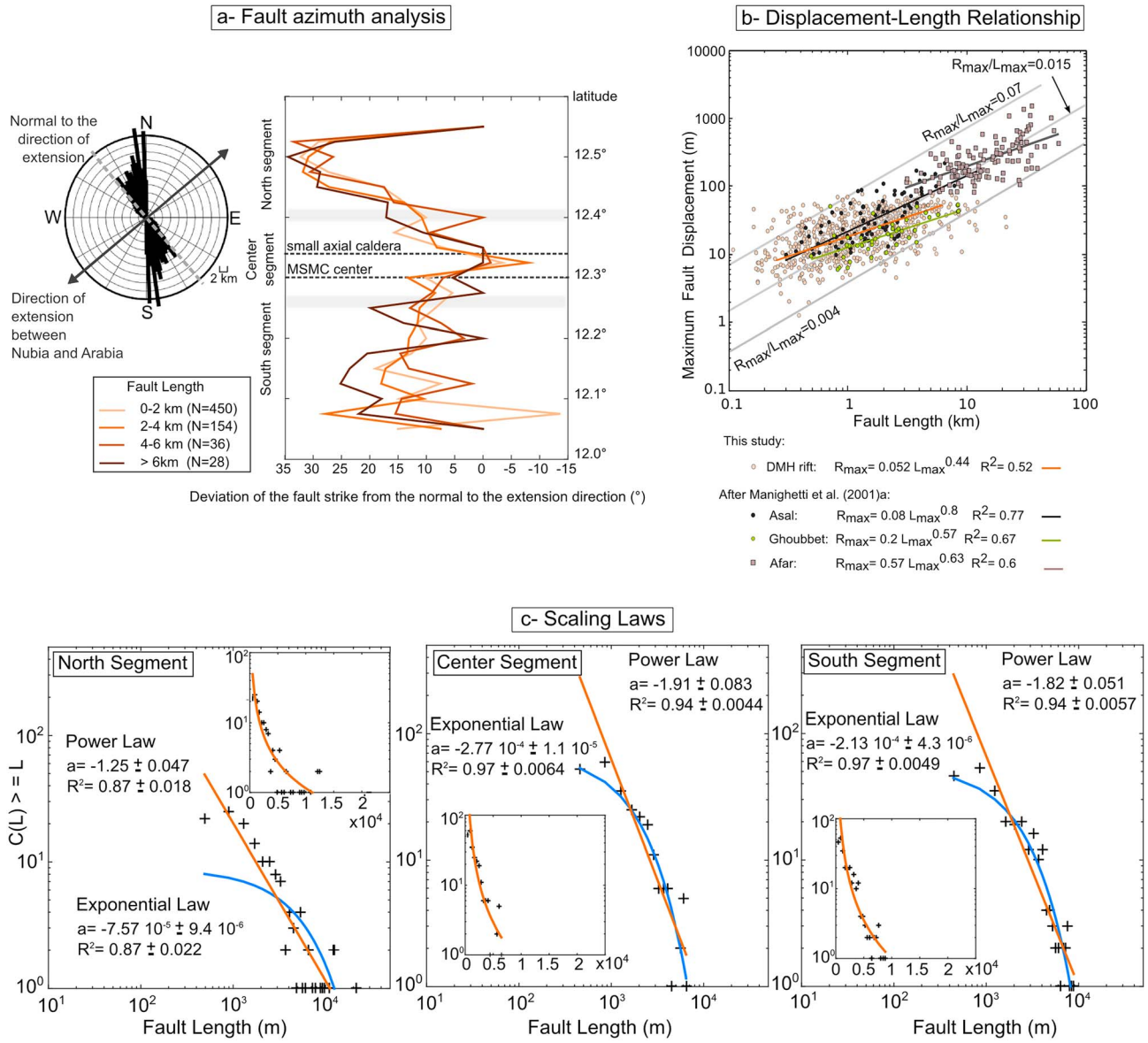


**Figure 4.** Fault attribute analysis including fault azimuth (a), displacement-length (D-L) relationship (b), and scaling laws (c). Analysis of fault azimuths (a) relies on a rose diagram (left) that represents the distribution of fault azimuth normalized by fault length and an obliquity plot (right) showing the deviation from the normal to the direction of extension plotted as a function of the latitude. The direction of extension at 49.3° (Dumont et al., 2017) is indicated as well as its normal (dashed line). For the obliquity plot (a), each fault is represented by its median latitude, length, and azimuth and then all faults were split into four groups depending on their length. (b) D-L measurements at DMH rift are compared to those of Central Afar, Asal, and Ghoubbet rifts (modified from Manighetti, King, et al., 2001). (c) Scaling laws are evaluated for fault length distribution for the segments north, center, and south located along Dabbahu-Manda-Hararo rift. For all segments, a cumulative distribution of fault length is presented in a log-log plot as well as a log-normal one (small insets). The parameters of both exponential (blue curves) or power laws (orange curves) are indicated on each plot.

for these kinds of fault measurements. However, as for the data of Asal-Ghoubbet and Central Afar, our data roughly aligns along slopes between 0.004 and 0.07. Thus, besides scattering, *D-L* measurements for DMH are more similar with measurements from Asal-Ghoubbet than with measurements derived from data from Central Afar that systematically yield higher ratio.

### 5.3. Scaling Laws

To account for the incompleteness of sampling or data discretization (Bonnet et al., 2001) for each of the three segments of DMH rift, we decided to analyze fault populations using two modes of representation, a

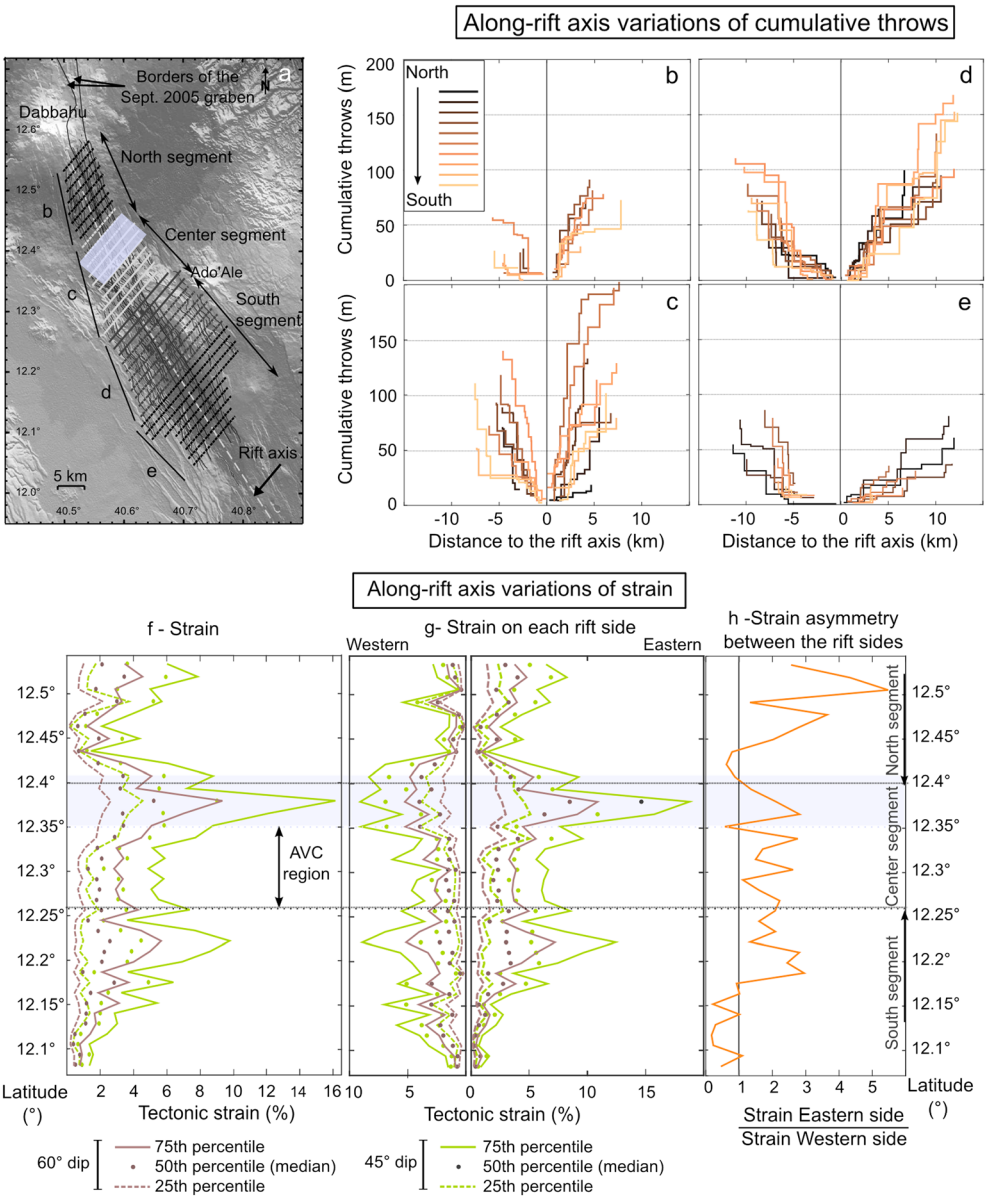


**Figure 5.** Along-rift axis variations of cumulative vertical throw and strain. Cumulative vertical throws are calculated along profiles normal to the direction of extension (a). The different gray tons are used to differentiate the (b)–(e) plots, while the dashed/full lines allow to identify if the profiles belong to the north, center, or south rift segments. The blue rectangle identifies profiles where the strain peak is observed in (f)–(g). (b–e) Cumulative vertical throws from the morphological rift axis toward rift margins. The degrading allows to locate the profiles from north to south on (a). (f) Strain estimates are deduced from the cumulative throws calculated along profiles shown in (a), (g) strain evaluated for the eastern and western rift flanks and (h) along-strike asymmetry calculated as the ratio between the strain on the eastern relative to the western flank. Strain is estimated for two end-member dips, for example, 60° (brown) and 45° (green). Filled lines represents the 75th percentiles of strain for each profile, dots the median, and dashed lines the 25th percentiles.

cumulative log-log plot of fault lengths and a cumulative log-normal plot (Figure 4c). The exponential and power laws represent the two end-members of fault growth processes. To estimate the law parameters, we used 300 bootstrap loops, each of them sampling randomly two thirds of the data (Efron & Tibshirani, 1986).

Using both representation modes, similar observations can be done for the central and south segments (Figure 4c), which are both sub-perpendicular to the regional extension direction. For these two data sets, exponential laws fit better the fault length distribution, while the power law only explains a part of the full fault length range we observe, with a high and low cutoff lengths. Conversely, the power law seems to

provide a better fit for most fault lengths in the north segment, which is oblique to the extension direction. The curvature in the log-log plot cannot be reproduced with a simple exponential model. The power law seems to preferentially fit data for lengths larger than ~1–1.5 km and up to 5–7.5 km, according to the log-normal plot, although it cannot explain the large number of long faults in the area. This scaling law analysis suggests that fault growth processes differ laterally along the DMH rift, with the north segment concentrating a large number of long faults.

## 6. Role of Faulting in Rifting Processes: Strain Estimates

Strain analysis along individual profiles show that regardless of the fault dip assumed, two thirds of the extension is accommodated along a narrow band that extends up to 2.5–5 km from the rift axis in the north and center segments (Figures 5a–5c). Southward, the width of this band increases to ~10–15 km, in an area where few faults are found near the rift axis (Figures 5d and 5e). This might be related to significant effusive volcanism covering faults and masking strain, or more distributed strain (Ferguson et al., 2010).

Figures 5f and 5g shows strain estimates based on fault dips of 45° and 60°, and its partition at both rift flanks to estimate asymmetry in extension (Figure 5h). The maximum strain along DMH rift is found at ~12.37°N, north of AVC in the center segment (Figure 5f) and estimated at ~12% and ~20% assuming a 60° and 45° dipping fault, respectively (Table 1). From this point, total strain decreases northward to reach a minimum (<2%) at ~12.44°N, to increase again toward Dabbahu volcano with median values of ~3% and 8%, for 60° and 45° dips, respectively (Figure 5f). South of the strain maximum, strain estimates are stable with median values of ~2% and ~5%, decreasing at the southern rift tip. In addition to along-axis variations in strain, there is a clear asymmetry, with the eastern flank displaying systematically higher strain than the western one (Table 1 and Figure 5h). This trend is reversed at the southern tip of the rift, as the western margin accommodates 2.5% to 3% and >5% of extension assuming fault dips of 60° and 45°, respectively, while the eastern margin accounts for ~1% and ~2.5% (Figure 5g). For the south segment, the maximum in tectonic strain is mostly accommodated at the eastern flank where it reaches ~10% and >15%, respectively, for 60° and 45° fault dips (Figure 5g and Table 1).

## 7. Discussion

### 7.1. Unusual Character of the North Rift Segment

The analysis of fault attributes highlight the difference in faulting patterns along the north segment of the DMH rift, relative to the center and south segments (Table 1). In the north, long faults appear at the rift center as well as on the rift margins (Figure 3 and supporting information, Figure S3). This observation is somehow unusual as faults grow both laterally and vertically from the rift center so that eventually the largest faults are located on the rift margins. Along DMH rift, dike intrusions accommodate most of the crustal extension, with dike-induced faulting contributing to fault growth (Belachew et al., 2013; Ebinger et al., 2008; Grandin et al., 2009; Hamling et al., 2009; Keir et al., 2011; Rowland et al., 2007). Actually, with repeated dike intrusions, faults migrate progressively away from the rift axis where more energy is required for faults to slip (Carbotte et al., 2006; Shaw & Lin, 1993). The presence of long faults at the rift center suggests that a different mechanism is driving fault growth along the north segment. Other processes allowing efficient fault lengthening may explain this observation, such as fault growth by linkage (Cartwright et al., 1995) or through damage zones (Kim et al., 2004). These along-rift axis variations in fault growth processes contribute also to the scattering of the *D-L* measurements (Kim & Sanderson, 2005). Other sources of *D-L* scattering include measurement errors, inelastic deformation, and to a lesser extent, local changes in material properties of the lithosphere (Cartwright et al., 1995; Kim & Sanderson, 2005).

With scaling laws, we have further analyzed fault growth processes over the three rift segments using two end-member models (Figure 4c): the power law distribution corresponding to a self-similar growth process thus scale independent, and exponential distributions that are scale dependent, and whose characteristic length is often linked to the elastic thickness of the lithosphere (Cowie & Shipton, 1998; Soliva & Schultz, 2008). Exponential and power laws have been both recognized at oceanic ridges and continental rifts (Bohnenstiehl & Carbotte, 2001; Bohnenstiehl & Kleinrock, 1999; Carbotte & Macdonald, 1994; Escartin et al., 1999; Scholz & Cowie, 1990). Exponential distributions best explain fault data at both the center and south segments of DMH rift (Figure 4c) and are generally interpreted as representing either an early extension stage (Bonnet et al., 2001) or high extension rates (Spyropoulos et al., 2002). In contrast, the

**Table 1**
*Summary of Fault Attributes and Their Variations in the Three Rift Segments Along the DMH Rift and at Lucky Strike Slow Spreading Ridge Segment*

| | Whole DMH ($N = 668$) | | | North segment ($N = 146$) | | | South segment ($N = 270$) | | | Center segment ($N = 252$) | | | Lucky Strike ($N = 1803$) | | |
|---|---|---|---|---|---|---|---|---|---|---|---|---|---|---|---|
| Fault length (km) | 1.9 ± 2.1 (1.2) | | | 2.6 ± 3.4 (1.4) | | | 1.9 ± 1.8 (1.3) | | | 1.4 ± 1.3 (1.0) | | | 0.25 ± 0.22 (0.19) | | |
| Length distribution | — | | | Mostly power law | | | Exponential law | | | Exponential law | | | Exponential law | | |
| Scarp height (m)[a] | 16.6 ± 11.9 (20.3) | | | 21.6 ± 14.1 (18.3) | | | 25.5 ± 17.4 (21.4) | | | 27.2 ± 19.0 (24.3) | | | — | | |
| $D_{max}/L$[b] | 0.011 (0.42)[e] | | | — | | | — | | | — | | | — | | |
| Azimuths (°) | 146.4 ± 28.6 (151.0) | | | 156.1 ± 35.8 (165.1) | | | 148.0 ± 22.7 (151.2) | | | 139.2 ± 27.8 (143.7) | | | 19.1 ± 13.7 (18.9) | | |
| Density (km/km$^2$)[c] | 0.87 ± 0.71 (med: 0.73, max: 7.1) | | | 1.2 ± 1.1 (med: 0.9, max: 7.1) | | | 0.83 ± 0.6 (med: 0.7, max: 3.6) | | | 0.7 ± 0.5 (med: 0.7, max: 3.2) | | | 3.47[g] | | |
| Tectonic strain[d] | W | E | All | W | E | All | W | E | All | W | E | All | W[f] | E[f] | All[f] |
| Med (%, 45° dip) | 2.0 | 3.7 | 3.1 | 2.4 | 2.8 | 3.5 | 2.7 | 1.4 | 2.5 | 3.3 | 4.15 | 4.45 | 12.3 | 9.3 | 11.9 |
| Max (%, 45° dip) | 13.9 | 20.2 | 20.2 | 8.8 | 13.2 | 13.2 | 11.0 | 16.7 | 16.7 | 13.9 | 20.2 | 20.2 | 12.3 | 11.8 | 12.3 |
| Med (%, 60° dip) | 1.2 | 2.2 | 1.8 | 1.4 | 1.6 | 2.0 | 1.5 | 0.8 | 1.4 | 1.9 | 2.4 | 2.6 | 7.1 | 5.3 | 6.9 |
| Max (%, 60° dip) | 8.0 | 11.7 | 11.7 | 5.1 | 7.6 | 7.6 | 6.3 | 9.7 | 9.7 | 8.0 | 11.7 | 11.7 | 7.1 | 6.8 | 6.9 |

*Note*. All values are presented as mean and their standard deviation and [median]; except when median (med) and maximum (max) are indicated. W for western flank, E for eastern one, All for both eastern and western flanks. DMH = Dabbahu-Manda-Hararo.
[a]Each fault is represented by its highest scarp height, the mean, std, median are applied to the whole fault population or the different segments. [b]$D$max/$L$ ratio estimated from a linear regression, with $R^2$ value indicated into brackets. [c]Fault density estimated as cumulative fault length per surface survey (2,062 km$^2$ for DMH rift, 119.6 km$^2$ for Lucky Strike). [d]Each profile is represented by a median and maximum strain values. [e]$D$max/$L$ estimate from Dumont (2013). [f]Derived from Figure 14 in Combier et al. (2015). [g]After Escartín et al. (2014).

power laws are considered to be representative of intermediate spreading rates (Spyropoulos et al., 2002) and correspond to lower amounts of deformation (Gupta & Scholz, 2000). Interestingly, only fault length distribution of the North segment cannot be clearly identified by one of these two laws (Figure 4c). These differences between the various rift segments, and especially differences with the north segment, demonstrate that the state of fault growth varies along the rift. If we consider the characteristic length of the exponential law as a proxy for elastic thickness (Cowie & Shipton, 1998) at the center and south segments, they indicate, respectively, 2.9 and 4.3 km; no such estimate can be obtained for the north segment. These estimates are much lower than the mean effective elastic thickness (Te) deduced from gravity and topographical data for the Afar region, which is on the order of 5–12 km (Ebinger & Hayward, 1996; Redfield et al., 2003). However, our estimates are consistent with values for thinned segments like Djibouti/Tadjura rift or the Danakil Depression where Te is 5–6 km (Ebinger & Hayward, 1996). Our values of elastic thickness is also in agreement at first order, with the detection of dike opening and shallow seismicity that barely exceed 5–6 km in depth nearby MSMC (Belachew et al., 2011; Grandin et al., 2012, and references therein). In contrast, for the north and south segments, dike opening was, respectively, detected down to ~12 and 10 km (Belachew et al., 2011; Grandin et al., 2012). Interestingly, the propagation rates during the 2006–2010 intrusive sequence also showed differences between the north and south segments, with faster rates observed for northward propagating dikes (Barnie et al., 2016; Belachew et al., 2011; Grandin et al., 2011). These observations point toward variations of the lithospheric conditions between the North and South segments, including both structural (thickness, thermal and internal structure) and dynamical properties (stress state; Barnie et al., 2016; Belachew et al., 2011; Dumont et al., 2017; Grandin et al., 2011, 2012). The results are therefore in good agreement with (1) a thicker brittle layer at segment ends than at the rift center where magma is stored and (2) a difference between the north and south segments reflecting a different lithospheric structure and state of stress. We interpret these differences as resulting from a less mature rifting stage in the north segment than in the south segment.

With the analysis of fault azimuths, we have shown that the largest azimuth deviations are located north of N12.45° (Figure 4a and supporting information, Figure S4). This is just north of the change of rift azimuth (Dumont, 2013) and north of the maximum tectonic strain detected along the rift (Figures 5f and 5g). Furthermore, Dumont (2013) made several observations along the north segment suggesting that faults in this area are more complex and sinuous than elsewhere along the rift. The authors observed also en échelon faulting and recognized some dextral strike-slip components along some faults, in agreement with some dextral strike-slip earthquakes detected in 1996 between the DMH and Alayta rifts (Hofstetter & Beyth, 2003). These observations, which provide long-term constraints on the extensional stresses, can be further compared with the current state of stress of the plate boundary using focal source mechanisms for the 1996–2010 period (Figure 6; Ayele et al., 2009; Barnie et al., 2016; Belachew et al., 2013; Ebinger et al.,

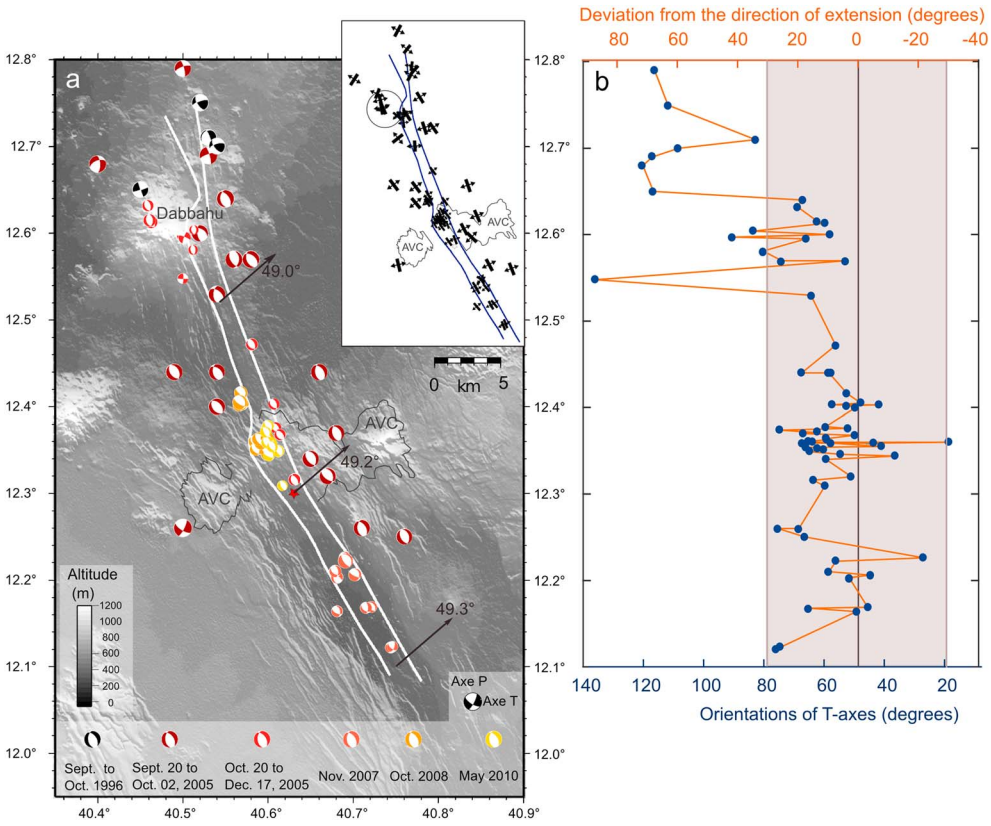


**Figure 6.** Fault plane solutions along Dabbahu-Manda-Hararo rift. (a) Fault plane solutions are lower hemisphere projections. Black and white beach balls represent global centroid-moment-tensor solutions for $M \geq 5.0$ events occurring in September and October 1996 (locations after Hofstetter & Beyth, 2003). Dark red and white beach balls correspond to solutions for $5.4 \geq M \geq 4.9$ events occurring mostly during September 2005 intrusion (locations after Ayele et al., 2009). Light red and white beach balls $2.9 < M < 3.9$ events occurred just after this main September 2005 intrusion and represent solutions from Ebinger et al. (2008). Beach balls accompanying November 2007 (south of mid-segment magma chamber) and October 2008 (north of mid-segment magma chamber) were associated with $3.4 \leq M \leq 4.6$ events with solutions from Belachew et al. (2013). Yellow beach balls are related to $3.3 \leq M \leq 3.7$ events accompanying May 2010 dike and eruption solutions from Barnie et al. (2016). Direction of extension between Nubia and Arabia plates is indicated along the three segments of Dabbahu-Manda-Hararo rift by arrows (after Vigny et al., 2006). The inset summarizes the minimum compressive stress σ3 (arrows) associated with all these focal mechanisms and the associated tension direction, σ1 being principally vertical downward. (b) *T* axes orientations (blue circles) corresponding to the focal mechanisms presented in (a). These directions are represented along the rift, as well as their deviation from the direction of extension (orange curve), N49° estimated after Vigny et al. (2006). The brownish area includes all deviations up to 30°, from N49°.

2008; Hofstetter & Beyth, 2003). These focal mechanisms are compatible with minimum horizontal compressive stress σ3 striking NE–SW south of ~12.55–12.6°N, illustrated by *T* axes orientations ranging from 20° and 80°N (Figure 6b). North of ~12.55°N, σ3 is more E-W oriented, as shown by deviations of the *T* axes by 60–80° with respect to the direction of extension (Figure 6b). These results evidence a rotation of the nodal planes in the vicinity of Dabbahu volcano, hence a local reorientation of stresses down to 12.55–12.6°N. Short- and long-term observations are therefore consistent within the first ~5 km from Dabbahu volcano. Largest deviations of the fault azimuths suggest that the reorientation of the local stresses initiates from ~12.45 to 12.5°N (Figure 4a), despite a limited number of faults mapped north of 12.5°N. The radius of influence of Dabbahu volcano would then extend to ~10–15 km. However, the few focal mechanisms determined between 12.45–12.55°N (Figure 6a) do not allow discussing whether the radius of influence of Dabbahu volcano differs, depending on whether instantaneous or finite strains are considered.

### 7.2. From Fault Growth to Rift Development

The *D*-*L* ratio of the DMH rift (Figure 4b) is similar to those measured along the Asal rift and Ghoubbet oceanic ridge (Manighetti, King, et al., 2001) where magmato-tectonic processes have been recognized (Doubre

et al., 2007; Doubre & Peltzer, 2007; Smittarello et al., 2016). Magmatic rift segments result therefore in similar fault populations. These *D-L* ratios including DMH, Asal, and Ghoubbet data are all clearly smaller than those of Central Afar, where extension is more distributed over a 70-km-wide band that links the rift segments of the Red Sea and Aden propagators (Figure 2a; Doubre et al., 2016; Manighetti, Tapponnier, et al., 2001). In Central Afar, the crust is ~18- to 25-km thick, with normal faults an order of magnitude larger than those at the DMH rift segment, such as in the Dôbi graben (Figure 4b; Hammond et al., 2011; Jacques et al., 2011). To a first order, the *D-L* fault ratios in the Afar region record different deformation modes and fault growth processes, as well as variations of the brittle-ductile transition.

The oldest dating of lavas, affected by rift faulting and located within a radius of 2 km from the DMH rift flank, goes back to ~0.1–0.2 Myr (Ferguson et al., 2013; Lahitte, Gillot, & Courtillot, 2003; Lahitte, Gillot, Kidane, et al., 2003). As the faulted area of DMH rift extends much further than the sites where these samples were taken, it suggests that the dismantling of AVC along both rift flanks started likely before and/or during the "Gulf Basalt" formation at ~1.1–0.6 Myr, facilitating the progressive ascent of basaltic magma toward the surface (Lahitte, Gillot, & Courtillot, 2003; Stab et al., 2016). The present-day rift axis seems therefore to have been shaped during the last 0.2 Myr by sporadic and intense magmato-tectonic phases which is consistent with recent dating and geological observations (Medynski et al., 2013, 2016; Rowland et al., 2007).

In the northernmost part of the rift, an intense effusive episode took place between ~72 and 58 kyr at Dabbahu volcano covering a broad area south of the volcanic edifice, corresponding mostly to our north segment (Figure 7; Field et al., 2013; Medynski et al., 2013). According to Medynski et al. (2013), this effusive episode might have started ~90–80 kyr ago. The subsequent decrease in the magma supply at Dabbahu (at ages younger than 50 kyr) contributed then to the edifice growth and dike-induced faulting along the southern flank of the volcano (Figure 7; Medynski et al., 2013). Moreover, combination of dating with structural analysis led Medynski et al. (2016) to highlight different displacement rates for faults located in the north segment according to their across-rift distance from the rift axis. The authors correlated these displacement rates with the distribution of magma from different sources along DMH rift (AVC at the rift center, Dabbahu and Gabho volcanoes, located north of the rift). They have shown that voluminous intrusions like the one of September 2005 under the eastern flank of the north rift segment (Figure 2b), were infrequent contrary to the ones along-axis. However dating shows that such a massive intrusion likely already occurred with a recurrence time of 5–10 kyr involving the three aforementioned magma sources (Medynski et al., 2016).

We propose that the link between the Dabbahu volcano and the Manda-Hararo rift segments was established only in recent times (few 10 kyr). The Dabbahu volcanic plumbing system has been maintained since the last ~60–70 kyr (Field et al., 2012, 2013; Medynski et al., 2013), contributing to the weakening of the surrounding brittle lithosphere by thermomechanical softening and therefore to the generation of a local stress concentration (Corti et al., 2003; Lahitte, Gillot, & Courtillot, 2003). This weakening effect, combined with the load of the volcanic edifice itself, could promote the capture of a propagating rift through the development of en-échelon and/or curved faults, as shown in analog models (van Wyk de Vries & Merle, 1996). Similar observations made in the north segment (Dumont, 2013) suggest that such a process may also have contributed to the DMH rift reorientation. This process may have been enhanced due to the short distance ($<$30 km) separating the Dabbahu volcano from the AVC that may have played a role in redefining locally the principal stress trajectory. A similar mechanical interaction was recognized for volcanic systems in central Iceland distant from 30 km on average (Gudmundsson & Andrew, 2007). The azimuth change taking place only between N12.35° and N12.45° suggests that Manda-Hararo rift already propagated several kilometers north of AVC, before the Dabbahu volcano was sufficiently developed to influence the local stress field and thus to capture Manda-Hararo rift propagation (Figure 7). The reorientation of focal mechanisms nearby Dabbahu volcano (Figure 6), as well as the absence of along-axis variations in the direction of extension, also supports this scenario (Dumont et al., 2017).

During the 2005–2010 rifting episode, dikes were intruded along two main trajectories north of AVC (Figures 2b, 3, and 7): (1) from AVC along the morphological rift axis, for most of the intrusive sequence and (2) from multiple interacting magma sources (Dabbahu, Gabho and AVC) and mostly along the eastern rift shoulder in the north segment (Ayele et al., 2009; Belachew et al., 2011, 2013; Grandin et al., 2009; Hamling et al., 2009; Wright et al., 2006). These two trajectories can also be seen in the fault density map (Figure 3). In the north segment, the two sectors characterized by a relative high fault density can be

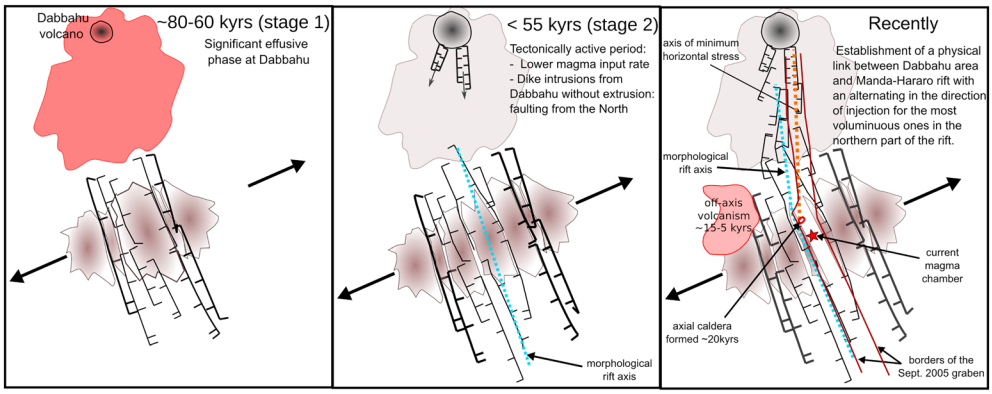


**Figure 7.** Conceptual model proposed for the evolution of Dabbahu-Manda-Hararo rift for the last ~100 kyr highlighting the influence of Dabbahu volcano in the development of Manda-Hararo rift. Details on the timing constraints are provided in the text.

tracked southward up to the rift center in a discontinuous manner. Both of them seem to bound past large intrusions equivalent to that of September 2005 but injected along axis (Rubin & Pollard, 1988). Interestingly, these two borders are highly asymmetrical with higher values directly south of Dabbahu (corresponding to the northwestern rift border, Figure 3). This observation is opposite to the asymmetry observed in the topography (Figures 1 and 2c) suggesting that other kind of intrusions, likely emitted only from Dabbahu volcano (Medynski et al., 2013), may also have contributed to this localized surface fracturing south of Dabbahu. The northeastern rift border although well defined, seems to be associated with values that extend further eastward but still confined within the September 2005 dike path and down to N12.44° of latitude (Figure 3). This more complex spatial pattern actually tends to confirm an unusual faulting distribution below the northeastern rift shoulder. It therefore confirms the existence and also the lower frequency of past off-axis large events with respect to large along-axis ones, in agreement with Medynski et al.'s (2016) conclusions. Such observation is also corroborated by cumulative slip profiles that indicate long-term southward propagation in the narrow band of the September 2015 intrusion in the north rift segment (Dumont et al., 2017). The sustained coexistence of these two trajectories in the north segment can be related to the three aforementioned sources of magma that interfere to distribute magma along this rift segment to release extensional stresses (Medynski et al., 2016). The fact that these two different trajectories do still coexist nowadays indicates that the zone of tectonic and magmatic activity is not yet fully localized and developed in this sector. Hence, with such a geometry, extensional stresses may not be released as efficiently as along the rest of the rift, explaining why the north segment may be at a less advanced rifting stage than elsewhere along the rift. So, along the north segment, the interference between dike intrusions coming from several different directions likely facilitates interaction of adjacent fault segments and therefore fault lengthening through linkage or damage zones (Cartwright et al., 1995; Kim et al., 2004), in contrast to areas where intrusions are emitted always from the same magma source and along similar directions, promoting lateral propagation of preexisting faults.

### 7.3. Comparison of DMH Rift and Mid-Oceanic Ridges for a Better Understanding of Continent-Ocean Transition

#### 7.3.1. DMH Rift and LS Spreading Oceanic Ridge: How Similar They Are?

The DMH rift has frequently been compared to slow-spreading oceanic ridge segments owing to several similarities, including morphology, extension rate, or magma storage (Hayward & Ebinger, 1996; Medynski et al., 2013). These systems also have numerous differences, which include lithospheric thickness, crustal structure, or plate boundary geometry and stress. Here we explore this analogy in more details using the example of Lucky Strike oceanic spreading segment (LS-OSS) along a slow-spreading ridge (Tables 1 and 2 and supporting information, Figure S5).

Located at 37.5°N along the Mid-Atlantic Ridge, this ~60-km-long spreading center shows a full spreading rate of ~20.3 mm/year, features that are comparable to those of the DMH rift (Figure 1; Gripp & Gordon, 1990; Vigny et al., 2006). Both segments show some asymmetry (Figure 1 and section 4). At LS-OSS, the

**Table 2**
*General Comparison of Characteristic Features Shared Between DMH Rift, LS-OSS, and Oceanic Ridges in General*

| Features | DMH | LS-OSS | DMH features similar to |
|---|---|---|---|
| Segment age | ~1–1.5 Myr[a] | ~10 Myr[b] | — |
| Extension/Spreading rate | ~15 mm/year[m] | ~20.3 mm/year[c] | S |
| Segment length | ~60 km | ~60 km | S, I[d] |
| Rift valley width | ~5–10 km | ~20 km | I |
| General morphology | axial basin | axial basin | S, I[d] |
| Maximum fault scarp heights (m) | ~100 | 500–900[e] | I, F |
| Fault length scaling law | Mostly exponential | exponential | S, I, F |
| Tectonic strain accommodated by faulting | ~10–20% | ~10% | S, I |
| Crust thickness at the segment center (km) | ~ 6[f] | ~7.5[e] | S, I, F |
| Crust thickness at the segment tips (km) | ~10–12 km[f,l] | ~5.5 [e)] | — |
| Depth of midsegment magma chamber (km) | ~4 and > 15[f] | ~3.5–6[b] | S |
| Lateral extension of the shallow magma chamber (km) | ~5–8[f] | ~ 6–7[b] | — |
| Along-axis shape of the shallow magma chamber | elongated | elongated | S, I, F[d] |
| Accretion process | Dike intrusion from the rift center[g] | Dike intrusion from the rift center[h] + detachment fault | S, I |
| Dike propagation rate | 0.5–3 km/hr[i] | | ~1–2 km S, I[i] |
| Basalt type | Not yet MORB[k] | E-MORB and T-MORB[j] | |
| $SiO_2$ content (wt.%) | 46.28–49.42 (*48.05–48.73*)[k] | 48.93–50 and 50.72–51.7[j] | |
| $K_2O/TiO_2$ | <0.25 (*<0.10*)[k] | >0.35 and <0.25[j] | |
| $La_n/Sm_n$ | 1.5–2.1 (*0.74–0.98*)[k] | 3.5–5 and 2–2.5[j] | |
| $^{87}Sr/^{86}Sr$ | 0.70362–0.70373 (*~0.70379*)[k] | 0.702941–0.703145 and 0.702874–0.703045[j] | |
| $^{143}Nd/^{143}Nd$ | Homogeneous: $\varepsilon_{Nd} = +5.2$ ($\varepsilon_{Nd} = +6$)[k] | $7.8 < \varepsilon_{Nd} < 8.4$ and $\varepsilon_{Nd} > 8.97$[j] | |
| $^{206}Pb/^{204}Pb$ | | 18.904 ± 0.06 and 19.199 ± 0.1[j] | |
| Basalt source | mantle contaminated by hydrothermally altered gabbroic cumulates (*presence of an ancient recycled oceanic crust component within the Ethiopian plume?*)[k] | Local heterogeneities in the composition of the depleted mantle showing refractory material and influence of the Azores mantle plume[j2] | |

*Note*. With I for intermediate oceanic ridges, S and F for slow (second-order discontinuities) and fast (third-order discontinuities) ones (from Carbotte et al., 2016). Isotopic compositions are presented to emphasize the mantle origins of the basalts at DMH rift and LS-OSS. E-MORB for enriched MORB, and T-MORB for transitional MORB, definition based on $K_2O/TiO_2$ and isotopic compositions (e.g., Gale et al., 2011). The composition indicated in italic for DMH basalts corresponds to the second type of basalt encountered along the rift, also named "the depleted Light Rare Earth Elements (LREE)" samples in Barrat et al. (2003).
[a]After Audin et al. (2004), Acocella et al. (2008). [b]After Singh et al., 2006; Escartín et al. (2014), and references therein. [c]After Escartin et al. (2001). [d]After Carbotte et al. (2016) and Macdonald (2001). [e]After Combier et al. (2015), and references therein. [f]After Grandin et al. (2010) and Belachew et al. (2011). [g]After Wright et al. (2006, 2012), Grandin et al. (2010). Hamling et al. (2009, 2010). [h]After Dziak et al. (2004). [i]After Grandin et al. (2011), and therein references. [j]After Hamelin et al. (2013) and Gale et al. (2011). [k]After Barrat et al. (2003) and Ferguson et al. (2013). [l]After Grandin et al. (2012), [m]Vigny et al. (2006), and references therein.

asymmetrical morphology is related to an asymmetrical accretion during the last 0.7 Myr (Escartin et al., 2001; Miranda et al., 2005), while at DMH rift, this asymmetry is caused by rifting processes (Svartman Dias et al., 2016). LS-OSS axial rift valley with a ~20-km width, approximately doubles that of the DMH rift valley (Figure 1), what might be partly due to the overall lithospheric structure and not necessarily due to the age difference between the two extensional systems, ~10 and <1.5 Myr, respectively (Table 2). Both LS-OSS and DMH rift host a series of volcanic constructs at the rift center that are intensely dissected by normal faulting (Figure 1). The LS-OSS hosts an active and recent ~10-km-diameter volcano, Lucky Strike, that rises 500 m above the surrounding seafloor at the segment center. Such a large volcanic edifice is not observed within the rift valley of DMH rift. The only individual volcanic structure is of smaller dimension, a ~1-km-diameter caldera formed about 20–25 kyr (Figures 1 and 2b; Medynski et al., 2015). However, melt is focused at both segment centers, likely associated with a comparable shallow magma plumbing system located at ~4- to 6-km depth and extending ~6–8 km along-axis and including both long-term and ephemeral magma bodies (Table 2; Belachew et al., 2011; Carbotte et al., 2016; Dumont et al., 2017; Grandin et al., 2010; Keir et al., 2009; Singh et al., 2006). At DMH rift, low-silica content, trace elements, and Nd, Sr isotopes do not reflect MORB-type melting regime but rather extension processes that are still evolving (Table 2; Barrat et al., 2003). On the contrary, LS-OSS basalts are clearly identified as MORB (Table 2; Gale et al., 2011; Hamelin et al., 2013). At the LS-OSS, both segment ends are bound by nontransform offsets, in areas where faulting dominates. This

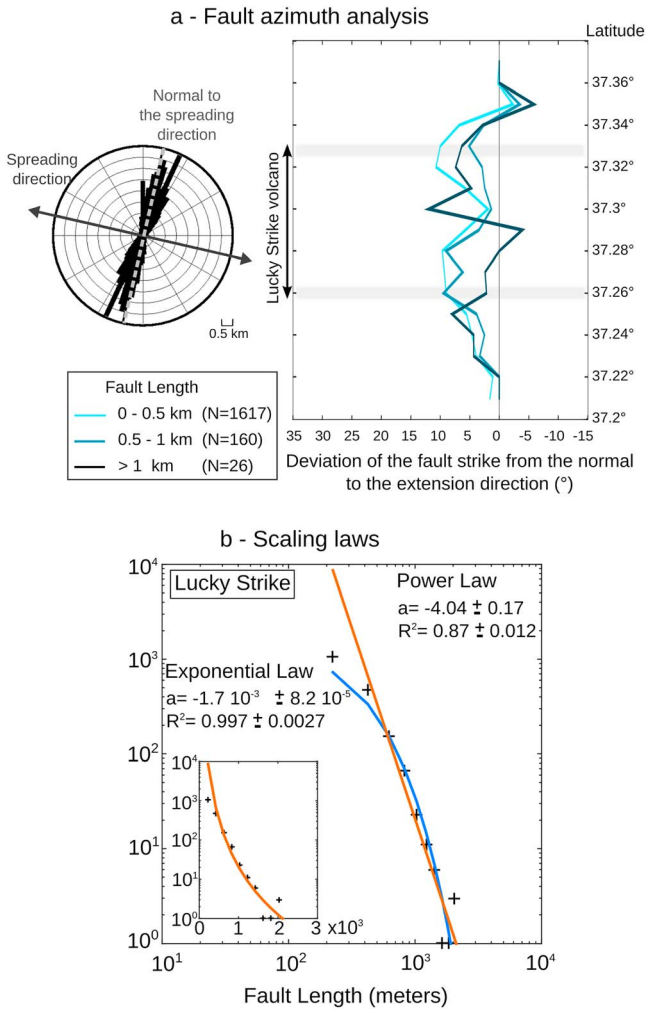


**Figure 8.** Fault attribute analysis including fault azimuth (a) and scaling laws (b) at Lucky Strike oceanic spreading segment using fault data from Escartin et al., (2015). Analysis of fault azimuths (a) is similar to that presented in Figure 4 for Dabbahu-Manda-Hararo rift, consisting of a rose diagram (left) and an obliquity plot (right) using the spreading direction of 103° (Escartin et al., 2001). For the scaling law analysis, the cumulative distribution of fault length is presented in a log-log plot as well as a log-normal one (small insets). The parameters of both exponential (blue curves) or power laws (orange curves) are indicated on each plot.

extension is associated with the exposure of ultramafic rocks outcrop, not observed anywhere else along the segment (Menez Hom, Figure 1). LS-OSS also lacks off-axis volcanism that has been identified at the DMH rift. Located NW in the Center segment (Figures 1 and 7; Medynski et al., 2015) and dated to ~15–5 kyr, the small volcanic edifice seems to stand at the apex of a large magma reservoir with a volume that would be 4 times larger than that of MSMC (Dessisa et al., 2013; Medynski et al., 2015).

Magma contributes also to localize crustal deformation at both extensional systems. At DMH rift, the rift valley narrows from ~8 to 5 km at the intersection of the rift axis with the AVC (Figure 1; Dumont et al., 2017), while the rift valley edges are not well defined, partly due to intense faulting. Such behavior is not clearly observed along the whole LS-OSS segment, although the neovolcanic zone crossing the LS volcano seems to behave similarly; it is narrower at the segment center (central volcano), becoming wider away from it (Figure 1; Escartín et al., 2014). Magmato-tectonic interactions have also been recognized at both DMH rift and LS-OSS. Magma intrusions contribute both to melt distribution from the segment center toward the segment ends and to fault growth, process that is also observed at intermediate spreading ridges (Carbotte et al., 2006, 2016; Dumont et al., 2016, 2017; Dziak et al., 2004; Escartín et al., 2014; Medynski et al., 2013, 2016; Rowland et al., 2007; Wright et al., 2012).

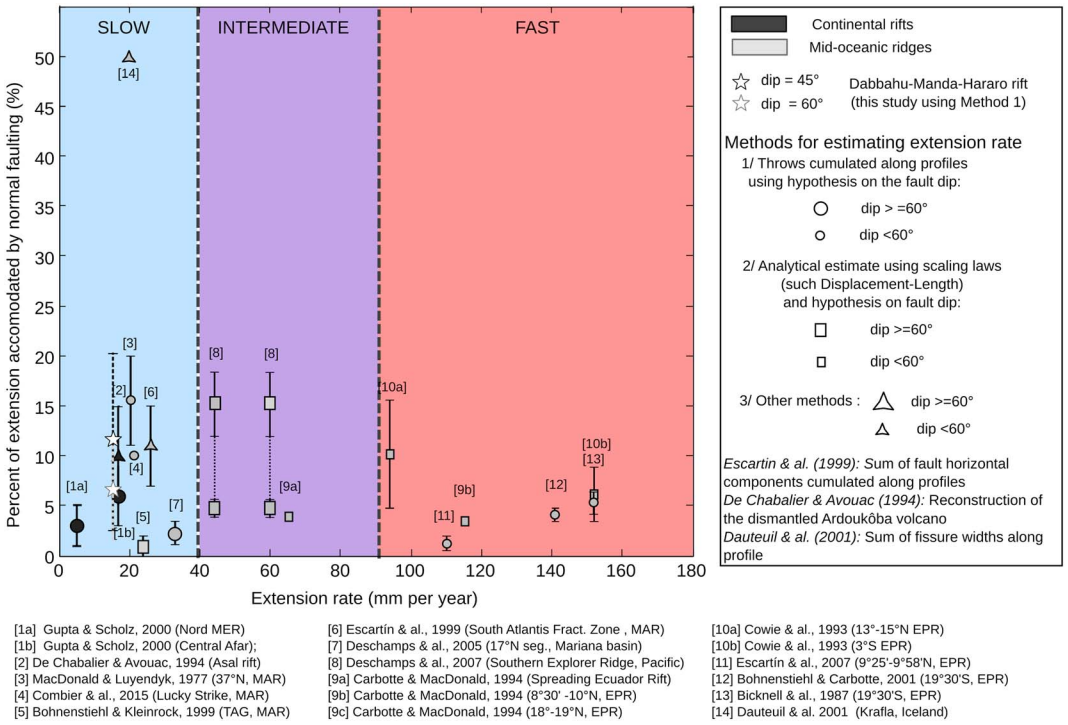


**Figure 9.** Comparison between strain rates accommodated by faulting at continental rifts and oceanic ridges as a function of the extension rate. The calculation method is designated through different symbols, with large symbols representing dip > 60° while small ones, dip < 60°. The color code indicates if it is a continental rift (dark gray) or oceanic ridge (light gray). Fault dip assumptions rely either on focal mechanisms of local earthquakes, other geophysical measurements and/or field observations, or are assumed.

The fault population of LS-OSS comprises rift bounding faults with vertical throws ranging from 500 to 900 m (Combier et al., 2015), while at the DMH rift they barely reach 100 m (Table 2; Figures 2b, 2c, and 5b–5e), comparable to those observed at intermediate and fast-spreading centers with thus a similar axial valley depth. We have further explored faulting at LS-OSS, using prior mapping of 1,803 faults identified from high-resolution (~10 m) sonar data (Escartin et al., 2015). This fault map that covers about one third of the total segment length centered around LS volcano (supporting information, Figure S5), including the transition from a narrow to a wider zone of deformation, is actually an analog to faults located in the center segment of DMH rift. Fault lengths at LS-OSS are very short (98.6% are <1 km, Figure 8a), with a mean length of 250 m, to be compared to 1.4 km at the DMH Center segment (Table 1), confirming that conditions for fault lengthening are at first order, not encountered in areas under permanent magma influence (Dumont et al., 2017). In addition, fault growth at LS-OSS and the center rift segment seems to be driven by similar processes as evidenced by exponential scaling laws also observed in the south segment of DMH rift (Figure 8b and Table 1). They mark a later stage in the evolution of the fault network (Spyropoulos et al., 2002) and are likely related to dike intrusions (Combier et al., 2015; Dziak et al., 2004; Rowland et al., 2007). Fault azimuth analyses reveal a much tighter clustering of azimuths normal to the spreading direction than those at DMH rift (Figures 8a and 4a), as illustrated with obliquity plots. Maximum obliquity, ~8–10° versus ~20–35° at DMH rift, is reached at the borders of LS volcano while it decreases outward, likely due to magma-induced localization.

Faulting at DMH rift and LS-OSS seems to have a similar contribution in rifting/spreading processes (Figure 9). There are numerous uncertainties and bias in methods used to estimate tectonic strain, for instance, fault dip assumption that can reduce strain estimate by 40% when using a 60° fault dip (Figure 5 and supporting information, Figure S2). In addition to these uncertainties, numerous other processes may impact fault analyses (e.g., erosion, fault dip angle, burial of faults by lava or sediment, and undetected faults), which would lead to an underestimate of tectonic strain estimates. Despite these limitations, the compilation of Figure 9 shows that faulting accommodates a modest fraction of the overall plate separation (~5–20%), across a wide range of spreading rates. Strain estimates are much more scattered for slow and

intermediate oceanic spreading centers, ranging from a few percent and up to 15–20% (Bohnenstiehl & Kleinrock, 1999; Carbotte & MacDonald, 1994; Combier et al., 2015; Dauteuil et al., 2001; Deschamps et al., 2005, 2007; Escartín et al., 1999; MacDonald & Luyendyck, 1977). On the contrary, they are consistently low, typically at ~5%, at fast oceanic ridges (Bicknell et al., 1987; Bohnenstiehl & Carbotte, 2001; Carbotte & MacDonald, 1994; Cowie et al., 1993; Escartín et al., 2007). For continental magmatic rifts, that have shown slow spreading rates, tectonic strain rarely exceeds 15% (De Chabalier & Avouac, 1994; Gupta & Scholz, 2000), except for the DMH rift when a 45° fault dip is assumed. In the center segment where the highest strain was estimated (Table 1), the maximum strain reaches ~12% for a 60° dip, while most median values along DMH rift do not exceed 3%. In addition, our fault mapping may not be exhaustive, contributing to a plausible underestimation of tectonic strain along the DMH rift. We thus estimate that faulting could represent up to 10–20% of strain along the DMH rift, therefore similar to strain estimates for Asal rift (De Chabalier & Avouac, 1994) or to those made at slow-spreading centers such as Lucky Strike (Combier et al., 2015).

#### 7.3.2. On the Continent-Ocean Transitional Rift

The comparison between the DMH rift and the LS-OSS oceanic segment provide clues to better understand the late stage of the continent-ocean transition at the DMH rift. We have shown that the upper crustal extension is accommodated similarly at both extensional systems. It is dominated by magmatic processes via dike intrusions injected from the segment center (~80%), in association with tectonic extension accommodated by normal faulting, not exceeding 10–20% of the total extension (Figure 9). In Afar and north of the Main Ethiopian rift, faulting is most exclusively related to dike intrusions as illustrated by high fault density centered on the magmatic centers (Agostini et al., 2011; Dumont et al., 2017). In the central and southern Main Ethiopian rift, the crustal extension is accommodated differently as evidenced by asymmetrical segments that develop from one large normal fault (Agostini et al., 2011; Hayward & Ebinger, 1996). At LS-OSS, a dichotomy exists in faulting processes as they are mainly dike-induced in the neovolcanic zone in the segment center and purely tectonic at segment ends (Combier et al., 2015; Seher et al., 2010). Additionally, both faulting and volcanic construction participate in shaping the DMH rift and LS-OSS morphology. Therefore, DMH rift and LS-OSS share first-order structural and kinematic features, suggesting that the spreading dynamics and its structural expression gets established during advanced/late stage of rifting (Keir et al., 2013).

Structural analyses points toward the existence of underplating at the base of the lower crust beneath the DMH rift (Stab et al., 2016). These results are supported by seismic studies, and in particular the ratio between the *P* and *S* wave velocities ($>2$), which indicates both melt and underplating (Hammond et al., 2011). The low-viscosity material associated with underplating is recognized as a key feature at volcanic passive margins (Geoffroy, 2005), which influences the response of the lithosphere to an extensional stress regime as suggested by numerical and analog modeling (Callot et al., 2001; Corti, 2012; Huismans & Beaumont, 2007). Thus, if the underplating material corresponds to a rheological boundary between the ductile lower crust and the brittle mantle, it contributes to form a narrow deformation zone and to localize the lithosphere breakup, as it is at DMH rift (Callot et al., 2001, and references therein). Models also suggest that this would result in a passive upwelling of the underlying mantle, with the development of shear zones connected to the underplating zone. Seismic velocity structure beneath Afar derived from relative travel time tomography does not show the Ethiopian mantle plume that initiated the continental breakup (Hammond et al., 2013, and references therein). Instead, it reveals low-velocity zones directly beneath irregular rift segments and down to 75-km depth, interpreted as shallow passive mantle upwelling rooted to the initial mantle plume. Midcrustal shear zones connected to the underplated material have also been suggested from the reconstruction of Central Afar cross section (Stab et al., 2016). All these observations we made at DMH rift considered together with results from numerical and analog modeling strongly suggest a decoupling of the lithospheric crust and mantle.

Understanding the behavior of the lithosphere is particularly important to unravel the processes controlling the transition from continental rifting to oceanic crust accretion. The lithospheric structure at magmatic slow-spreading ridges likely shows an along-axis variation, with a thicker lithosphere at the segment ends that includes lithospheric upper mantle (e.g., Cannat et al., 2009). At the segment center, both the long-term melt supply and the presence of transient melt lenses suggest a much thinner lithosphere, likely restricted to the magmatic crust. This is supported by the presence of a ~3-km-deep melt lens at LS-OSS (Singh et al., 2006) underlain by seismic crustal velocities that are anomalously low and interpreted as a crustal volume at high-temperature, and/or containing small amounts of melt (Seher et al., 2010). Thus, a decoupling of the lithospheric crust and mantle characterizes segment centers at LS-OSS and slow oceanic ridges,

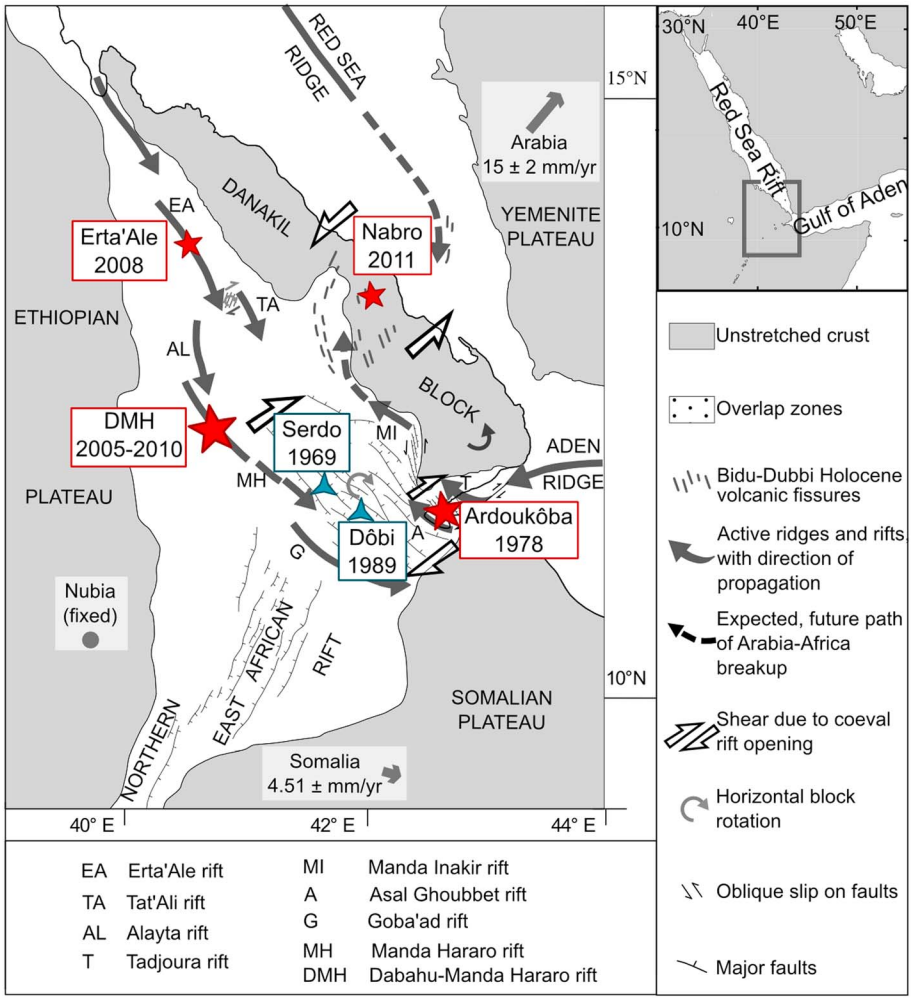


**Figure 10.** Location of magmatic crises (red stars) and seismic ones (blue triangles) in Central Afar since the twentieth century. In background, tectonic map after Figure 26 of Manighetti, Tapponnier, et al. (2001).

similarly as at DMH rift (Grandin et al., 2012). However, this decoupling evolves to become fully coupled at segment ends of slow-spreading ridges (Grandin et al., 2012; Seher et al., 2010).

The narrow rift stage, currently observed at DMH rift, follows a phase of wide rifting, identified in Central Afar (Stab et al., 2016). Such a phase is consistent with the general evolution of the continent-ocean transition (Buck, 1991; Péron-Pinvidic et al., 2013), whereas it contributes to the debate on the evolution of the Afar depression (Audin et al., 2004; Manighetti et al., 1998; Wolfenden et al., 2004). The thinning stage is characterized by the transition from a decoupled to coupled crustal/mantle extension (Brun, 2002; Cannat et al., 2009; Péron-Pinvidic et al., 2013; Svartman Dias et al., 2015, 2016). North of DMH rift, Keir et al., (2013) showed a drastic change in segment morphology, crustal and mantle structure, as well as faulting and magmatic processes. Lithospheric thinning northward seems thus to play a key role in these changes and especially the significantly reduced lower crust thickness beneath the Danakil depression (Bastow & Keir, 2011; Hammond et al., 2011; Keir et al., 2013). The decoupling/coupling transition is therefore at a different stage, likely more advanced, in northern Afar than at DMH rift, although the extension rate is slightly lower (Pagli et al., 2012). Rifting processes appear therefore to depend on crustal thickness variations making the extension depth dependent. This depth-dependent extension likely influences the thermal regime of the lithosphere and/or vice versa. Whatever the source of these lithospheric variations, either the thermal conditions or the rifting processes, they impact the strain rate, the surface morphology, and also the rheology and hence the variations in the brittle-ductile transition (Cannat et al., 2009; Grandin et al., 2012; Keir et al., 2013; Svartman Dias et al., 2016). No correlation between rift morphology, extension rate

and magma is observed in the Afar depression (supporting information, Table S1). Actually, the absence of such correlation for the Afar depression, is also observed at slow-spreading ridges and in particular at LS-OSS, due to their small extension rates and their lower thermal gradient (Morgan & Ghen, 1993). In spite of this, oceanic ridges including slow-spreading ridges show durable morphologies, reflecting stable thermal conditions in the lithosphere, contrary to continental magmatic rifts. At slow-spreading ridges, these thermal conditions rely on a balance between the heat supply and cooling (Cannat et al., 2009). This balance likely varies along a ridge segment from center to ends, similarly to the degree of lithospheric coupling and to the tectonic deformation that increases toward segment ends, involving in some cases detachment faulting (Grandin et al., 2012; Seher et al., 2010). At DMH rift, the inheritance of continental crust mixed with newly accreted mafic material contributes to transitional thermal conditions, as also illustrated by geochemical compositions and in particular isotopes that are used as tracers of mantle dynamics (Table 2). Moreover, it is difficult to further discuss the along-rift variations in faulting processes at DMH rift, the variation in the balance of magmatic and tectonic processes being only partly documented (Dumont et al., 2016, 2017; Grandin et al., 2010, 2011; Hamling et al., 2009; Medynski et al., 2013, 2016; Rowland et al., 2007). The depth-dependent extension and feedback thus likely determine the transitional present-day surface expression of DMH rift and also that of other rift segments in a late rifting stage.

This transient behavior of DMH rift may also be integrated at the scale of the Afar depression (Figure 10). During the twentieth century, the episodic release of tectonic stresses mostly by magma intrusions (Asal rift in 1978, Ruegg & Kasser, 1987; DMH rift in 2005–2010, Wright et al., 2012), and also through seismic sequences (Serdo and Dôbi in 1969 and 1989, respectively, Kebede et al., 1989; Jacques et al., 2011) reveals an axis joining the RS and GA propagators, where extensional stresses are released at the scale of the whole depression. GA and RS branches form the main boundaries of the triple junction, which is in agreement with GPS (Doubre et al., 2016) and InSAR measurements (Pagli et al., 2014). These magmatic and tectonic events may also represent a transient phase of stress release that are part of large-scale cycles operating at time scales of several thousand years and contributing to the transition toward the oceanic spreading.

## 8. Conclusions

We quantified fault attributes (azimuth, length, and throw) for 668 normal faults to analyze fault growth processes and strain distribution along Dabbahu-Manda-Hararo rift (Central Afar, Ethiopia). This analysis allowed us to document along-axis variations in fault growth processes, as well as in rift morphology. North of the transversal AVC volcanic chain and between N12.35° and N12.45°, the azimuth of DMH rift changes accommodated by the fault population. In addition of being characterized by faults trending almost north-south, the northern part of the rift also shows long faults distributed evenly at the rift axis and margins. Combined to scaling laws and morphological analysis, these results suggest specificities of the northern part of the rift that cannot be explained by regional processes such as changes in the direction of extension between Nubia and Arabia tectonic plates. Instead, all the observations point toward the influence of Dabbahu volcano in the rift development. Using thermomechanical arguments, we suggest that crustal magma chambers act as stress concentrators. We propose that the propagating Manda-Hararo rift was captured in the last ~100 kyr by the Dabbahu volcano. We also link rifting processes at DMH rift as representative of a late rifting stage at the continent-ocean transition through the comparison of characteristic features of DMH rift to those of the slow oceanic spreading center Lucky Strike located in North Atlantic. By integrating these observations with numerical and analogous modeling, this approach allows us to discuss the transient features of the late stage of rifting and their origin.

**Acknowledgments**
This research benefited from fruitful discussions with Jean-Bernard De Chabalier. We thank the Editors, Derek Keir and Nicholas W. Hayman for their constructive reviews that significantly improved this manuscript. Most figures were prepared using the Generic Mapping Tool (GMT) software by Wessel and Smith (1991) Wessel et al. (2013) and Inkscape. This research was performed during S. Dumont's PhD thesis at IPGP (France) and was supported by the French Agence Nationale pour la Recherche (DoRA project, ANR-09-JCJC-0051e01). S. Dumont is currently supported by FCT through the postdoctoral grant (SFRH/BPD/17714/2016), as part of POCH and the European Union. Data used in this study can be obtained in the references and also requested from the corresponding author. This is IPGP contribution 3999.

## References

Acocella, V. (2014). Structural control on magmatism along divergent and convergent plate boundaries: Overview, model, problems. *Earth-Science Reviews*, *136*, 226–288. https://doi.org/10.1016/j.earscirev.2014.05.006

Acocella, V., Abebe, B., Korme, T., & Barberi, F. (2008). Structure of Tendaho graben and Manda Hararo rift: Implications for the evolution of the southern Red Sea propagator in Central Afar. *Tectonics*, *27*, TC4016. https://doi.org/10.1029/2007TC002236

Agostini, A., Bonini, M., Corti, G., Sani, F., & Mazzarini, F. (2011). Fault architecture in the Main Ethiopian rift and comparison with experimental models: Implications for rift evolution and Nubia–Somalia kinematics. *Earth and Planetary Science Letters*, *301*(3–4), 479–492. https://doi.org/10.1016/j.epsl.2010.11.024

Audin, L., Quidelleur, X., Coulié, E., Courtillot, V., Gilder, S., Manighetti, I., et al. (2004). Palaeomagnetism and K-Ar and $^{40}Ar/^{39}Ar$ ages in the Ali Sabieh area (Republic of Djibouti and Ethiopia): Constraints on the mechanism of Aden ridge propagation into southeastern Afar during the last 10 Myr. *Geophysical Journal International*, *158*(1), 327–345. https://doi.org/10.1111/j.1365-246X.2004.02286.x

Ayele, A., Jacques, E., Kassim, M., Kidane, T., Omar, A., Tait, S., et al. (2007). The volcano–seismic crisis in Afar, Ethiopia, starting September 2005. *Earth and Planetary Science Letters*, *255*(1–2), 177–187. https://doi.org/10.1016/j.epsl.2006.12.014

Ayele, A., Keir, D., Ebinger, C., Wright, T. J., Stuart, G. W., Buck, W. R., et al. (2009). September 2005 mega-dike emplacement in the Manda-Harraro nascent oceanic rift (Afar depression). *Geophysical Research Letters*, *36*, L20306. https://doi.org/10.1029/2009GL039605

Barberi, F., & Varet, J. (1977). Volcanism of Afar: Small-scale plate tectonics implications. *Geological Society of America Bulletin*, *88*(9), 1251–1266.

Barnie, T. D., Keir, D., Hamling, I., Hofmann, B., Belachew, M., Carn, S., et al. (2016). A multidisciplinary study of the final episode of the Manda Hararo dyke sequence, Ethiopia, and implications for trends in volcanism during the rifting cycle. *Geological Society, London, Special Publications*, *420*(1), 149–163. https://doi.org/10.1144/SP420.6

Barrat, J. A., Joron, J. L., Taylor, R. N., Fourcade, S., Nesbitt, R. W., & Jahn, B. M. (2003). Geochemistry of basalts from Manda Hararo, Ethiopia: LREE-depleted basalts in Central Afar. *Lithos*, *69*(1), 1–13. https://doi.org/10.1016/S0024-4937(03)00044-6

Bastow, I. D., & Keir, D. (2011). The protracted development of the continent–ocean transition in Afar. *Nature Geoscience*, *4*(4), 248. https://doi.org/10.1038/ngeo1095

Behn, M. D., Lin, J., & Zuber, M. T. (2002). A continuum mechanics model for normal faulting using a strain-rate softening rheology: Implications for thermal and rheological controls on continental and oceanic rifting. *Earth and Planetary Science Letters*, *202*(3–4), 725–740. https://doi.org/10.1016/S0012-821X(02)00792-6

Belachew, M., Ebinger, C., & Coté, D. (2013). Source mechanisms of dike-induced earthquakes in the Dabbahu-Manda Hararo rift segment in Afar, Ethiopia: Implications for faulting above dikes. *Geophysical Journal International*, *192*(3), 907–917. https://doi.org/10.1093/gji/ggs076

Belachew, M., Ebinger, C., Coté, D., Keir, D., Rowland, J. V., Hammond, J. O., & Ayele, A. (2011). Comparison of dike intrusions in an incipient seafloor-spreading segment in Afar, Ethiopia: Seismicity perspectives. *Journal of Geophysical Research*, *116*, B06405. https://doi.org/10.1029/2010JB007908

Bicknell, J. D., Sempere, J. C., Macdonald, K. C., & Fox, P. J. (1987). Tectonics of a fast spreading center: A Deep-Tow and Sea Beam survey on the East Pacific rise at 19°30′S. *Marine Geophysical Researches*, *9*(1), 25–45.

Bohnenstiehl, D. R., & Carbotte, S. M. (2001). Faulting patterns near 19°30′S on the East Pacific rise: Fault formation and growth at a superfast spreading center. *Geochemistry, Geophysics, Geosystems*, *2*(9), 1056. https://doi.org/10.1029/2001GC000156

Bohnenstiehl, D. R., & Kleinrock, M. C. (1999). Faulting and fault scaling on the median valley floor of the trans-Atlantic geotraverse (TAG) segment, ~26°N on the mid-Atlantic ridge. *Journal of Geophysical Research*, *104*(B12), 29,351–29,364.

Bonnet, E., Bour, O., Odling, N. E., Davy, P., Main, I., Cowie, P., & Berkowitz, B. (2001). Scaling of fracture systems in geological media. *Reviews of Geophysics*, *39*(3), 347–383. https://doi.org/10.1029/1999RG000074

Brun, J. P. (2002). Deformation of the continental lithosphere: Insights from brittle-ductile models. *Geological Society, London, Special Publications*, *200*(1), 355–370. https://doi.org/10.1144/GSL.SP.2001.200.01.20

Buck, W. R. (1991). Modes of continental lithospheric extension. *Journal of Geophysical Research*, *96*(B12), 20,161–20,178.

Buck, W. R. (2004). Consequences of asthenospheric variability on continental rifting. In G. D. Karner, N. W. Driscoll, B. Taylor, & D. L. Kohlstedt (Eds.), *Rheology and deformation of the lithosphere at continental margins* (pp. 1–30). New York: Columbia University Press.

Callot, J. P., Grigné, C., Geoffroy, L., & Brun, J. P. (2001). Development of volcanic passive margins: Two-dimensional laboratory models. *Tectonics*, *20*(1), 148–159. https://doi.org/10.1029/2000TC900030

Cannat, M., Briais, A., Deplus, C., Escartín, J., Georgen, J., & Lin, J. (1999). Mid-Atlantic ridge–Azores hotspot interactions: Along-axis migration of a hotspot-derived event of enhanced magmatism 10 to 4 Ma ago. *Earth and Planetary Science Letters*, *173*(3), 257–269.

Cannat, M., Manatschal, G., Sauter, D., & Peron-Pinvidic, G. (2009). Assessing the conditions of continental breakup at magma-poor rifted margins: What can we learn from slow spreading mid-ocean ridges? *Comptes Rendus Geoscience*, *341*(5), 406–427. https://doi.org/10.1016/j.crte.2009.01.005

Carbotte, S. M., Detrick, R. S., Harding, A., Canales, J. P., Babcock, J., Kent, G., et al. (2006). Rift topography linked to magmatism at the intermediate spreading Juan de Fuca ridge. *Geology*, *34*(3), 209–212. https://doi.org/10.113/G21969.1

Carbotte, S. M., & Macdonald, K. C. (1994). Comparison of seafloor tectonic fabric at intermediate, fast, and super fast spreading ridges: Influence of spreading rate, plate motions, and ridge segmentation on fault patterns. *Journal of Geophysical Research*, *99*(B7), 13,609–13,631.

Carbotte, S. M., Smith, D. K., Cannat, M., & Klein, E. M. (2016). Tectonic and magmatic segmentation of the Global Ocean ridge system: A synthesis of observations. *Geological Society, London, Special Publications*, *420*(1), 249–295. https://doi.org/10.1144/SP420.5

Cartwright, J. A., Trudgill, B. D., & Mansfield, C. S. (1995). Fault growth by segment linkage: An explanation for scatter in maximum displacement and trace length data from the Canyonlands grabens of SE Utah. *Journal of Structural Geology*, *17*(9), 1319–1326.

Casey, M., Ebinger, C., Keir, D., Gloaguen, R., & Mohamed, F. (2006). Strain accommodation in transitional rifts: Extension by magma intrusion and faulting in Ethiopian rift magmatic segments. *Geological Society, London, Special Publications*, *259*(1), 143–163. https://doi.org/10.1144/GSL.SP.2006.259.01.13

Chorowicz, J. (2005). The east African rift system. *Journal of African Earth Sciences*, *43*(1–3), 379–410. https://doi.org/10.1016/j.jafrearsci.2005.07.019

Combier, V., Seher, T., Singh, S. C., Crawford, W. C., Cannat, M., Escartín, J., & Dusunur, D. (2015). Three-dimensional geometry of axial magma chamber roof and faults at Lucky Strike volcano on the Mid-Atlantic ridge. *Journal of Geophysical Research: Solid Earth*, *120*, 5379–5400. https://doi.org/10.1002/2015JB012365

Corti, G. (2012). Evolution and characteristics of continental rifting: Analog modeling-inspired view and comparison with examples from the east African rift system. *Tectonophysics*, *522*, 1–33. https://doi.org/10.1016/j.tecto.2011.06.010

Corti, G., Van Wijk, J., Bonini, M., Sokoutis, D., Cloetingh, S., Innocenti, F., & Manetti, P. (2003). Transition from continental break-up to punctiform seafloor spreading: How fast, symmetric and magmatic. *Geophysical Research Letters*, *30*(12), 1604. https://doi.org/10.1029/2003GL017374

Courtillot, V. (1982). Propagating rifts and continental breakup. *Tectonics*, *1*(3), 239–250.

Courtillot, V., Jaupart, C., Manighetti, I., Tapponnier, P., & Besse, J. (1999). On causal links between flood basalts and continental breakup. *Earth and Planetary Science Letters*, *166*(3–4), 177–195. https://doi.org/10.1016/S0012-821X(98)00282-9

Cowie, P. A., & Scholz, C. H. (1992a). Growth of faults by accumulation of seismic slip. *Journal of Geophysical Research*, *97*(B7), 11,085–11,095.

Cowie, P. A., & Scholz, C. H. (1992b). Physical explanation for the displacement-length relationship of faults using a post-yield fracture mechanics model. *Journal of Structural Geology*, *14*(10), 1133–1148.

Cowie, P. A., Scholz, C. H., Edwards, M., & Malinverno, A. (1993). Fault strain and seismic coupling on mid-ocean ridges. *Journal of Geophysical Research*, *98*(B10), 17,911–17,920.

Cowie, P. A., & Shipton, Z. K. (1998). Fault tip displacement gradients and process zone dimensions. *Journal of Structural Geology*, *20*(8), 983–997.

Dauteuil, O., Angelier, J., Bergerat, F., Verrier, S., & Villemin, T. (2001). Deformation partitioning inside a fissure swarm of the northern Icelandic rift. *Journal of Structural Geology*, *23*(9), 1359–1372. https://doi.org/10.1016/S0191-8141(01)00002-5

De Chabalier, J. B., & Avouac, J. P. (1994). Kinematics of the Asal rift (Djibouti) determined from the deformation of Fieale volcano. *Science*, *265*(5179), 1677–1681.

Deschamps, A., Fujiwara, T., Asada, M., Montesi, L., & Gente, P. (2005). Faulting and volcanism in the axial valley of the slow-spreading center of the Mariana back arc basin from Wadatsumi side-scan sonar images. *Geochemistry, Geophysics, Geosystems*, *6*, Q05006. https://doi.org/10.1029/2004GC000881

Deschamps, A., Tivey, M., Embley, R. W., & Chadwick, W. W. (2007). Quantitative study of the deformation at southern explorer ridge using high-resolution bathymetric data. *Earth and Planetary Science Letters*, *259*(1–2), 1–17. https://doi.org/10.1016/j.epsl.2007.04.007

Desissa, M., Johnson, N. E., Whaler, K. A., Hautot, S., Fisseha, S., & Dawes, G. J. K. (2013). A mantle magma reservoir beneath an incipient mid-ocean ridge in Afar, Ethiopia. *Nature Geoscience*, *6*(10), 861. https://doi.org/10.1038/ngeo1925

Didana, Y. L., Thiel, S., & Heinson, G. (2014). Magnetotelluric imaging of upper crustal partial melt at Tendaho graben in Afar, Ethiopia. *Geophysical Research Letters*, *41*, 3089–3095. https://doi.org/10.1002/2014GL060000

Doubre, C., Deprez, A., Masson, F., Socquet, A., Lewi, E., Grandin, R., et al. (2016). Current deformation in Central Afar and triple junction kinematics deduced from GPS and InSAR measurements. *Geophysical Journal International*, *208*(2), 936–953. https://doi.org/10.1093/gji/ggw434

Doubre, C., Manighetti, I., Dorbath, L., Dorbath, C., Bertil, D., & Delmond, J. C. (2007). Crustal structure and magmato-tectonic processes in an active rift (Asal-Ghoubbet, Afar, East Africa): 2. Insights from the 23-year recording of seismicity since the last rifting event. *Journal of Geophysical Research*, *112*, B05406. https://doi.org/10.1029/2006JB004333

Doubre, C., & Peltzer, G. (2007). Fluid-controlled faulting process in the Asal rift, Djibouti, from 8 yr of radar interferometry observations. *Geology*, *35*(1), 69–72. https://doi.org/10.1130/G23022A.1

Dumont, S. (2013). Étude de la relation entre les déformations tectoniques long et court-terme d'un rift magmatique pour la compréhension des mécanismes de rifting : cas du Manda-Hararo (Afar éthiopien). PhD thesis: Institut de Physique du Globe de Paris, 350 p.

Dumont, S., Klinger, Y., Socquet, A., Doubre, C., & Jacques, E. (2017). Magma influence on propagation of normal faults: Evidence from cumulative slip profiles along Dabbahu-Manda-Hararo rift segment (Afar, Ethiopia). *Journal of Structural Geology*, *95*, 48–59. https://doi.org/10.1016/j.jsg.2016.12.008

Dumont, S., Socquet, A., Grandin, R., Doubre, C., & Klinger, Y. (2016). Surface displacements on faults triggered by slow magma transfers between dyke injections in the 2005–2010 rifting episode at Dabbahu–Manda–Hararo rift (Afar, Ethiopia). *Geophysical Journal International*, *204*(1), 399–417. https://doi.org/10.1093/gji/ggv449

Dziak, R. P., Smith, D. K., Bohnenstiehl, D. R., Fox, C. G., Desbruyeres, D., Matsumoto, H., et al. (2004). Evidence of a recent magma dike intrusion at the slow spreading Lucky Strike segment, mid-Atlantic ridge. *Journal of Geophysical Research*, *109*, B12102. https://doi.org/10.1029/2004JB003141

Ebinger, C. J., & Casey, M. (2001). Continental breakup in magmatic provinces: An Ethiopian example. *Geology*, *29*(6), 527–530.

Ebinger, C. J., & Hayward, N. J. (1996). Soft plates and hot spots: Views from Afar. *Journal of Geophysical Research*, *101*(B10), 21,859–21,876.

Ebinger, C. J., Keir, D., Ayele, A., Calais, E., Wright, T. J., Belachew, M., et al. (2008). Capturing magma intrusion and faulting processes during continental rupture: Seismicity of the Dabbahu (Afar) rift. *Geophysical Journal International*, *174*(3), 1138–1152. https://doi.org/10.1111/j.1365-246X.2008.03877.x

Ebinger, C. J., Keir, D., Bastow, I. D., Whaler, K., Hammond, J. O., Ayele, A., et al. (2017). Crustal structure of active deformation zones in Africa: Implications for global crustal processes. *Tectonics*, *36*, 3298–3332. https://doi.org/10.1002/2017TC004526

Efron, B., & Tibshirani, R. (1986). Bootstrap methods for standard errors, confidence intervals, and other measures of statistical accuracy. *Statistical Science 1*(1), 54–75.

Ehrhardt, A., & Hübscher, C. (2015). The northern Red Sea in transition from rifting to drifting-lessons learned from ocean deeps. In *The Red Sea* (pp. 99–121). Berlin, Heidelberg: Springer.

Escartin, J., Cannat, M., Pouliquen, G., Rabain, A., & Lin, J. (2001). Crustal thickness of V-shaped ridges south of the Azores: Interaction of the mid-Atlantic ridge (36–39 N) and the Azores hot spot. *Journal of Geophysical Research*, *106*(B10), 21,719–21,735. https://doi.org/10.1029/2001JB000224

Escartin, J., Cowie, P. A., Searle, R. C., Allerton, S., Mitchell, N. C., MacLeod, C. J., & Slootweg, A. P. (1999). Quantifying tectonic strain and magmatic accretion at a slow spreading ridge segment, mid-Atlantic ridge, 29°N. *Journal of Geophysical Research*, *104*(B5), 10,421–10,437.

Escartin, J., Fornari, D., & Humphris, S. (2015). Extent of faults and fissures at the mid-Atlantic ridge-Lucky Strike vent field derived from sidescan sonar data acquired during the Knorr expedition KN145–19 (1996). *Interdisciplinary Earth Data Alliance (IEDA)*. https://doi.org/10.1594/IEDA/321461

Escartín, J., Soule, S. A., Cannat, M., Fornari, D. J., Düşünür, D., & Garcia, R. (2014). Lucky Strike seamount: Implications for the emplacement and rifting of segment-centered volcanoes at slow spreading mid-ocean ridges. *Geochemistry, Geophysics, Geosystems*, *15*, 4157–4179. https://doi.org/10.1002/2014GC005477

Escartín, J., Soule, S. A., Fornari, D. J., Tivey, M. A., Schouten, H., & Perfit, M. R. (2007). Interplay between faults and lava flows in construction of the upper oceanic crust: The East Pacific rise crest 9°25′–9°58′ N. *Geochemistry, Geophysics, Geosystems*, *8*, Q06005. https://doi.org/10.1029/2006GC001399

Ferguson, D. J., Barnie, T. D., Pyle, D. M., Oppenheimer, C., Yirgu, G., Lewi, E., et al. (2010). Recent rift-related volcanism in Afar, Ethiopia. *Earth and Planetary Science Letters*, *292*(3-4), 409–418. https://doi.org/10.1016/j.epsl.2010.02.010

Ferguson, D. J., Calvert, A. T., Pyle, D. M., Blundy, J. D., Yirgu, G., & Wright, T. J. (2013). Constraining timescales of focused magmatic accretion and extension in the Afar crust using lava geochronology. *Nature Communications*, *4*, 1416. https://doi.org/10.1038/ncomms2410

Field, L., Blundy, J., Brooker, R. A., Wright, T., & Yirgu, G. (2012). Magma storage conditions beneath Dabbahu volcano (Ethiopia) constrained by petrology, seismicity and satellite geodesy. *Bulletin of Volcanology*, *74*(5), 981–1004. https://doi.org/10.1007/s00445-012-0580-6

Field, L., Blundy, J., Calvert, A., & Yirgu, G. (2013). Magmatic history of Dabbahu, a composite volcano in the Afar rift, Ethiopia. *Bulletin*, *125*(1–2), 128–147. https://doi.org/10.1130/B30560.1

Gale, A., Escrig, S., Gier, E. J., Langmuir, C. H., & Goldstein, S. L. (2011). Enriched basalts at segment centers: The Lucky Strike (37°17′ N) and Menez Gwen (37°50′ N) segments of the mid-Atlantic ridge. *Geochemistry, Geophysics, Geosystems*, *12*, Q06016. https://doi.org/10.1029/2010GC003446

Gallacher, R. J., Keir, D., Harmon, N., Stuart, G., Leroy, S., Hammond, J. O., et al. (2016). The initiation of segmented buoyancy-driven melting during continental breakup. *Nature Communications*, *7*(1), 13110. https://doi.org/10.1038/ncomms13110

Geoffroy, L. (2005). Volcanic passive margins. *Comptes Rendus Geoscience*, *337*(16), 1395–1408. https://doi.org/10.1016/j.crte.2005.10.006

Grandin, R., Jacques, E., Nercessian, A., Ayele, A., Doubre, C., Socquet, A., et al. (2011). Seismicity during lateral dike propagation: Insights from new data in the recent Manda Hararo–Dabbahu rifting episode (Afar, Ethiopia). *Geochemistry, Geophysics, Geosystems*, *12*, Q0AB08. https://doi.org/10.1029/2010GC003434

Grandin, R., Socquet, A., Binet, R., Klinger, Y., Jacques, E., de Chabalier, J. B., et al. (2009). September 2005 Manda Hararo-Dabbahu rifting event, Afar (Ethiopia): Constraints provided by geodetic data. *Journal of Geophysical Research*, *114*, B08404. https://doi.org/10.1029/2008JB005843

Grandin, R., Socquet, A., Doin, M. P., Jacques, E., de Chabalier, J. B., & King, G. C. P. (2010). Transient rift opening in response to multiple dike injections in the Manda Hararo rift (Afar, Ethiopia) imaged by time-dependent elastic inversion of interferometric synthetic aperture radar data. *Journal of Geophysical Research*, *115*, B09403. https://doi.org/10.1029/2009JB006883

Grandin, R., Socquet, A., Doubre, C., Jacques, E., & King, G. C. (2012). Elastic thickness control of lateral dyke intrusion at mid-ocean ridges. *Earth and Planetary Science Letters*, *319*, 83–95. https://doi.org/10.1016/j.epsl.2011.12.011

Gripp, A. E., & Gordon, R. G. (1990). Current plate velocities relative to the hotspots incorporating the NUVEL-1 global plate motion model. *Geophysical Research Letters*, *17*(8), 1109–1112.

Gudmundsson, A., & Andrew, R. E. (2007). Mechanical interaction between active volcanoes in Iceland. *Geophysical Research Letters*, *34*, L10310. https://doi.org/10.1029/2007GL029873

Gupta, A., & Scholz, C. H. (2000). Brittle strain regime transition in the Afar depression: Implications for fault growth and seafloor spreading. *Geology*, *28*(12), 1087–1090.

Hamelin, C., Bezos, A., Dosso, L., Escartin, J., Cannat, M., & Mevel, C. (2013). Atypically depleted upper mantle component revealed by Hf isotopes at lucky strike segment. *Chemical Geology*, *341*, 128–139. https://doi.org/10.1016/j.chemgeo.2013.01.013

Hamling, I. J., Ayele, A., Bennati, L., Calais, E., Ebinger, C. J., Keir, D., et al. (2009). Geodetic observations of the ongoing Dabbahu rifting episode: New dyke intrusions in 2006 and 2007. *Geophysical Journal International*, *178*(2), 989–1003. https://doi.org/10.1111/j.1365-246X.2009.04163.x

Hamling, I. J., Wright, T. J., Calais, E., Lewi, E., & Fukahata, Y. (2014). InSAR observations of post-rifting deformation around the Dabbahu rift segment, Afar, Ethiopia. *Geophysical Journal International*, *197*(1), 33–49. https://doi.org/10.1093/gji/ggu003

Hammond, J. O., Kendall, J. M., Stuart, G. W., Ebinger, C. J., Bastow, I. D., Keir, D., et al. (2013). Mantle upwelling and initiation of rift segmentation beneath the Afar depression. *Geology*, *41*(6), 635–638. https://doi.org/10.1130/G33925.1

Hammond, J. O., Kendall, J. M., Stuart, G. W., Keir, D., Ebinger, C., Ayele, A., & Belachew, M. (2011). The nature of the crust beneath the Afar triple junction: Evidence from receiver functions. *Geochemistry, Geophysics, Geosystems*, *12*, Q12004. https://doi.org/10.1029/2011GC003738

Hayward, N. J., & Ebinger, C. J. (1996). Variations in the along-axis segmentation of the Afar rift system. *Tectonics*, *15*(2), 244–257.

Hofmann, C., Courtillot, V., Feraud, G., Rochette, P., Yirgu, G., Ketefo, E., & Pik, R. (1997). Timing of the Ethiopian flood basalt event and implications for plume birth and global change. *Nature*, *389*(6653), 838.

Hofstetter, R., & Beyth, M. (2003). The Afar depression: Interpretation of the 1960–2000 earthquakes. *Geophysical Journal International*, *155*(2), 715–732. https://doi.org/10.1046/j.1365-246X.2003.02080.x

Huismans, R. S., & Beaumont, C. (2007). Roles of lithospheric strain softening and heterogeneity in determining the geometry of rifts and continental margins. *Geological Society, London, Special Publications*, *282*(1), 111–138. https://doi.org/10.1144/SP282.6

Jacques, E., Kidane, T., Tapponnier, P., Manighetti, I., Gaudemer, Y., Meyer, B., et al. (2011). Normal faulting during the August 1989 earthquakes in Central Afar: Sequential triggering and propagation of rupture along the Dôbi graben. *Bulletin of the Seismological Society of America*, *101*(3), 994–1023. https://doi.org/10.1785/0120080317

Kebede, F., Kim, W. Y., & Kulhánek, O. (1989). Dynamic source parameters of the March-May 1969 Serdo earthquake sequence in Central Afar, Ethiopia, deduced from teleseismic body waves. *Journal of Geophysical Research*, *94*(B5), 5603–5614.

Keir, D., Bastow, I. D., Pagli, C., & Chambers, E. L. (2013). The development of extension and magmatism in the Red Sea rift of Afar. *Tectonophysics*, *607*, 98–114. https://doi.org/10.1016/j.tecto.2012.10.015

Keir, D., Belachew, M., Ebinger, C. J., Kendall, J. M., Hammond, J. O., Stuart, G. W., et al. (2011). Mapping the evolving strain field during continental breakup from crustal anisotropy in the Afar depression. *Nature Communications*, *2*(1), 285. https://doi.org/10.1038/ncomms1287

Keir, D., Ebinger, C. J., Stuart, G. W., Daly, E., & Ayele, A. (2006). Strain accommodation by magmatism and faulting as rifting proceeds to breakup: Seismicity of the northern Ethiopian rift. *Journal of Geophysical Research*, *111*, B05314. https://doi.org/10.1029/2005JB003748

Keir, D., Hamling, I. J., Ayele, A., Calais, E., Ebinger, C., Wright, T. J., et al. (2009). Evidence for focused magmatic accretion at segment centers from lateral dike injections captured beneath the Red Sea rift in Afar. *Geology*, *37*(1), 59–62. https://doi.org/10.1130/G25147A.1

Kidane, T., Courtillot, V., Manighetti, I., Audin, L., Lahitte, P., Quidelleur, X., et al. (2003). New paleomagnetic and geochronologic results from Ethiopian Afar: Block rotations linked to rift overlap and propagation and determination of a ~2 ma reference pole for stable Africa. *Journal of Geophysical Research*, *108*(B2), 2102. https://doi.org/10.1029/2001JB000645

Kim, Y. S., Peacock, D. C., & Sanderson, D. J. (2004). Fault damage zones. *Journal of Structural Geology*, *26*(3), 503–517. https://doi.org/10.1016/j.jsg.2003.08.002

Kim, Y. S., & Sanderson, D. J. (2005). The relationship between displacement and length of faults: A review. *Earth-Science Reviews*, *68*(3–4), 317–334. https://doi.org/10.1016/j.earscirev.2004.06.003

Kogan, L., Fisseha, S., Bendick, R., Reilinger, R., McClusky, S., King, R., & Solomon, T. (2012). Lithospheric strength and strain localization in continental extension from observations of the east African rift. *Journal of Geophysical Research*, *117*, B03402. https://doi.org/10.1029/2011JB008516

Kolyukhin, D., & Torabi, A. (2012). Statistical analysis of the relationships between faults attributes. *Journal of Geophysical Research*, *117*, B05406. https://doi.org/10.1029/2011JB008880

Kusznir, N. J., & Karner, G. D. (2007). Continental lithospheric thinning and breakup in response to upwelling divergent mantle flow: Application to the Woodlark, Newfoundland and Iberia margins. *Geological Society, London, Special Publications*, *282*(1), 389–419. https://doi.org/10.1144/SP282.16

Lahitte, P., Gillot, P. Y., & Courtillot, V. (2003). Silicic central volcanoes as precursors to rift propagation: The Afar case. *Earth and Planetary Science Letters*, *207*(1–4), 103–116. https://doi.org/10.1016/S0012-821X(02)01130-5

Lahitte, P., Gillot, P. Y., Kidane, T., Courtillot, V., & Bekele, A. (2003). New age constraints on the timing of volcanism in Central Afar, in the presence of propagating rifts. *Journal of Geophysical Research*, *108*(B2), 2123. https://doi.org/10.1029/2001JB001689

Liao, J., & Gerya, T. (2015). From continental rifting to seafloor spreading: Insight from 3D thermo-mechanical modeling. *Gondwana Research*, *28*(4), 1329–1343. https://doi.org/10.1016/j.gr.2014.11.004

Macdonald, K. C. (2001). Mid-ocean ridge tectonics, volcanism and geomorphology. *Encyclopedia of Ocean Sciences*, 1798–1813. https://doi.org/10.1006/rwos.2001.0094

MacDonald, K. C., & Luyendyk, B. P. (1977). Deep-tow studies of the structure of the mid-Atlantic ridge crest near lat 37°N. *Geological Society of America Bulletin*, *88*(5), 621–636.

Manighetti, I., King, G. C. P., Gaudemer, Y., Scholz, C. H., & Doubre, C. (2001). Slip accumulation and lateral propagation of active normal faults in Afar. *Journal of Geophysical Research*, *106*(B7), 13,667–13,696. https://doi.org/10.1029/2000JB900471

Manighetti, I., Tapponnier, P., Courtillot, V., Gallet, Y., Jacques, E., & Gillot, P. Y. (2001). Strain transfer between disconnected, propagating rifts in Afar. *Journal of Geophysical Research*, *106*(B7), 13,613–13,665. https://doi.org/0.1029/2000JB900454

Manighetti, I., Tapponnier, P., Gillot, P. Y., Jacques, E., Courtillot, V., Armijo, R., et al. (1998). Propagation of rifting along the Arabia-Somalia plate boundary: Into Afar. *Journal of Geophysical Research*, *103*(B3), 4947–4974. https://doi.org/10.1029/97JB02758

Medynski, S., Pik, R., Burnard, P., Dumont, S., Grandin, R., Williams, A., et al. (2016). Magmatic cycles pace tectonic and morphological expression of rifting (Afar depression, Ethiopia). *Earth and Planetary Science Letters*, *446*, 77–88. https://doi.org/10.1016/j.epsl.2016.04.014

Medynski, S., Pik, R., Burnard, P., Vye-Brown, C., France, L., Schimmelpfennig, I., et al. (2015). Stability of rift axis magma reservoirs: Spatial and temporal evolution of magma supply in the Dabbahu rift segment (Afar, Ethiopia) over the past 30 kyr. *Earth and Planetary Science Letters*, *409*, 278–289. https://doi.org/10.1016/j.epsl.2014.11.002

Medynski, S., Pik, R., Burnard, P., Williams, A., Vye-Brown, C., Ferguson, D., et al. (2013). Controls on magmatic cycles and development of rift topography of the Manda Hararo segment (Afar, Ethiopia): Insights from cosmogenic 3He investigation of landscape evolution. *Earth and Planetary Science Letters*, *367*, 133–145. https://doi.org/10.1016/j.epsl.2013.02.006

Miranda, J. M., Luis, J. F., Lourenço, N., & Santos, F. M. (2005). Identification of the magnetization low of the Lucky Strike hydrothermal vent using surface magnetic data. *Journal of Geophysical Research*, *110*, B04013. https://doi.org/10.1029/2004JB003085

Morgan, J. P., & Ghen, Y. J. (1993). Dependence of ridge-axis morphology on magma supply and spreading rate. *Nature*, *364*(6439), 706.

Pagli, C., Wang, H., Wright, T. J., Calais, E., & Lewi, E. (2014). Current plate boundary deformation of the Afar rift from a 3-D velocity field inversion of InSAR and GPS. *Journal of Geophysical Research: Solid Earth*, *119*, 8562–8575. https://doi.org/10.1002/2014JB011391

Pagli, C., Wright, T. J., Ebinger, C. J., Yun, S. H., Cann, J. R., Barnie, T., & Ayele, A. (2012). Shallow axial magma chamber at the slow-spreading Erta Ale ridge. *Nature Geoscience*, *5*(4), 284. https://doi.org/10.1038/ngeo1414

Péron-Pinvidic, G., Manatschal, G., & Osmundsen, P. T. (2013). Structural comparison of archetypal Atlantic rifted margins: A review of observations and concepts. *Marine and Petroleum Geology*, *43*, 21–47. https://doi.org/10.1016/j.marpetgeo.2013.02.002

Perrin, C., Manighetti, I., Ampuero, J. P., Cappa, F., & Gaudemer, Y. (2016). Location of largest earthquake slip and fast rupture controlled by along-strike change in fault structural maturity due to fault growth. *Journal of Geophysical Research: Solid Earth*, *121*, 3666–3685. https://doi.org/10.1002/2015JB012671

Redfield, T. F., Wheeler, W. H., & Often, M. (2003). A kinematic model for the development of the Afar depression and its paleogeographic implications. *Earth and Planetary Science Letters*, *216*(3), 383–398. https://doi.org/10.1016/S0012-821X(03)00488-6

Rooney, T. O., Bastow, I. D., Keir, D., Mazzarini, F., Movsesian, E., Grosfils, E. B., et al. (2014). The protracted development of focused magmatic intrusion during continental rifting. *Tectonics*, *33*, 875–897. https://doi.org/10.1002/2013TC003514

Rowland, J. V., Baker, E., Ebinger, C. J., Keir, D., Kidane, T., Biggs, J., et al. (2007). Fault growth at a nascent slow-spreading ridge: 2005 Dabbahu rifting episode, Afar. *Geophysical Journal International*, *171*(3), 1226–1246. https://doi.org/10.1111/j.1365-246X.2007.03584.x

Rubin, A. M., & Pollard, D. D. (1988). Dike-induced faulting in rift zones of Iceland and Afar. *Geology*, *16*(5), 413–417.

Ruegg, J. C., & Kasser, M. (1987). Deformation across the Asal-Ghoubbet rift, Djibouti, uplift and crustal extension 1979–1986. *Geophysical Research Letters*, *14*(7), 745–748.

Scholz, C. H. (2002). *The mechanics of earthquakes and faulting*. Cambridge: Cambridge University Press.

Scholz, C. H., & Cowie, P. A. (1990). Determination of total strain from faulting using slip measurements. *Nature*, *346*(6287), 837.

Seher, T., Crawford, W. C., Singh, S. C., Cannat, M., Combier, V., & Dusunur, D. (2010). Crustal velocity structure of the Lucky Strike segment of the mid-Atlantic ridge at 37°N from seismic refraction measurements. *Journal of Geophysical Research*, *115*, B03103. https://doi.org/10.1029/2009JB006650

Shaw, P. R., & Lin, J. (1993). Causes and consequences of variations in faulting style at the mid-Atlantic ridge. *Journal of Geophysical Research*, *98*(B12), 21,839–21,851.

Singh, S. C., Crawford, W. C., Carton, H., Seher, T., Combier, V., Cannat, M., et al. (2006). Discovery of a magma chamber and faults beneath a mid-Atlantic ridge hydrothermal field. *Nature*, *442*(7106), 1029–1032. https://doi.org/10.1038/nature05105

Smittarello, D., Grandin, R., De Chabalier, J. B., Doubre, C., Deprez, A., Masson, F., et al. (2016). Transient deformation in the Asal-Ghoubbet rift (Djibouti) since the 1978 diking event: Is deformation controlled by magma supply rates? *Journal of Geophysical Research: Solid Earth*, *121*, 6030–6052. https://doi.org/10.1002/2016JB013069

Soliva, R., & Schultz, R. A. (2008). Distributed and localized faulting in extensional settings: Insight from the north Ethiopian rift–Afar transition area. *Tectonics*, *27*, TC2003. https://doi.org/10.1029/2007TC002148

Spyropoulos, C., Scholz, C. H., & Shaw, B. E. (2002). Transition regimes for growing crack populations. *Physical Review E*, *65*(5), 056105. https://doi.org/10.1103/PhysRevE.65.056,105

Stab, M., Bellahsen, N., Pik, R., Quidelleur, X., Ayalew, D., & Leroy, S. (2016). Modes of rifting in magma-rich settings: Tectono-magmatic evolution of Central Afar. *Tectonics*, *35*, 2–38. https://doi.org/10.1002/2015TC003893

Stein, R. S., Briole, P., Ruegg, J. C., Tapponnier, P., & Gasse, F. (1991). Contemporary, Holocene, and quaternary deformation of the Asal rift, Djibouti: Implications for the mechanics of slow spreading ridges. *Journal of Geophysical Research*, *96*(B13), 21,789–21,806.

Svartman Dias, A. E., Hayman, N. W., & Lavier, L. L. (2016). Thinning factor distributions viewed through numerical models of continental extension. *Tectonics*, *35*, 3050–3069. https://doi.org/10.1002/2016TC004266

Svartman Dias, A. E., Lavier, L. L., & Hayman, N. W. (2015). Conjugate rifted margins width and asymmetry: The interplay between lithospheric strength and thermomechanical processes. *Journal of Geophysical Research: Solid Earth*, *120*, 8672–8700. https://doi.org/10.1002/2015JB012074

Torabi, A., & Berg, S. S. (2011). Scaling of fault attributes: A review. *Marine and Petroleum Geology*, *28*(8), 1444–1460. https://doi.org/10.1016/j.marpetgeo.2011.04.003

van Wyk de Vries, B., & Merle, O. (1996). The effect of volcanic constructs on rift fault patterns. *Geology*, *24*(7), 643–646.

Vigny, C., Huchon, P., Ruegg, J. C., Khanbari, K., & Asfaw, L. M. (2006). Confirmation of Arabia plate slow motion by new GPS data in Yemen. *Journal of Geophysical Research*, *111*, B02402. https://doi.org/10.1029/2004JB003229

Wessel, P., & Smith, W. H. F. (1991). Free software helps map and display data. *Eos, Transactions American Geophysical Union*, *72*, 441.

Wessel, P., Smith, W. H. F., Scharroo, R., Luis, J. F., & Wobbe, F. (2013). Generic mapping tools: Improved version released. *Eos, Transactions American Geophysical Union*, *94*, 409–410.

Wolfenden, E., Ebinger, C., Yirgu, G., Deino, A., & Ayalew, D. (2004). Evolution of the northern Main Ethiopian rift: Birth of a triple junction. *Earth and Planetary Science Letters*, *224*(1–2), 213–228. https://doi.org/10.1016/j.epsl.2004.04.022

Wright, T. J., Ebinger, C., Biggs, J., Ayele, A., Yirgu, G., Keir, D., & Stork, A. (2006). Magma-maintained rift segmentation at continental rupture in the 2005 Afar dyking episode. *Nature*, *442*(7100), 29. https://doi.org/10.1038/nature04978

Wright, T. J., Sigmundsson, F., Pagli, C., Belachew, M., Hamling, I. J., Brandsdóttir, B., Keir, D., et al. (2012). Geophysical constraints on the dynamics of spreading centres from rifting episodes on land. *Nature Geoscience*, *5*(4), 242–250. https://doi.org/10.1038/ngeo1428